Pergamon

Geochimica et Cosmochimica Acta, Vol. 61, No. 23, pp. 5065–5088, 1997

0016-7037/97 $17.00 + .00

PII S0016-7037(97)00305-0

Noble gases, their carrier phases, and argon chronology of upper mantle rocks from Zabargad Island, Red Sea

M. TRIELOFF,[1] H. W. WEBER,[2] G. KURAT,[3] E. K. JESSBERGER,[1,*] and J. JANICKE[1]

[1]Max-Planck-Institut für Kernphysik, D-69029 Heidelberg, Germany
[2]Max-Planck-Institut für Chemie, D-55122 Mainz, Germany
[3]Naturhistorisches Museum, A-1014 Wien, Austria

(*Received November* 14, 1996; *accepted in revised form August* 13, 1997)

Abstract—Three ultramafic bodies on Zabargad Island contain fresh peridotites with mostly unfractionated primitive bulk major and trace element abundances and mostly monomineralic vein rocks (pyroxenites, olivinites, hornblendites, etc.). We analyzed a set of coarse grained vein rocks with the ^{40}Ar-^{39}Ar technique applying high resolution stepheating. Neutron induced argon isotopes derived from Ca, K, and Cl, and the specific degassing behaviour of major and accessory minerals enabled us to separate and identify different trapped and radiogenic argon components and their hosts. Within two clinopyroxenites trapped argon is present in (1) low temperature, low $^{40}Ar/^{36}Ar$ phases (serpentine and/or fluid inclusions), (2) pyroxene-related Cl-rich carriers (pyroxene and/or associated microinclusions), and (3) amphiboles which are intimately and nonseparably intergrown with pyroxene. The amphiboles, which can texturally, chemically, and isotopically be divided into different generations, formed by interaction of spinels and pyroxenes with mantle fluids during different stages of diapiric uplift (Agrinier et al., 1993). Formation of these amphiboles and microinclusions in pyroxenes, along with incorporation of isotopically distinct Ar with $^{40}Ar/^{36}Ar$ ratios up to 8000, can be related to recent mantle metasomatism also evident in Arabian xenoliths (Henjes-Kunst et al., 1990) and must have been induced by a variety of mantle fluids. For a hornblendite, in situ radiogenic and excess argon components could be separated: the plateau age of 18.7 ± 1.3 Ma is in perfect agreement with a zircon Pb/Pb age of 18.4 ± 1.0 Ma (Oberli et al., 1987) interpreted as the age of crustal intrusion. Obviously, the formation of the hornblendite occurred during the final stage of uplift, most probably by interaction with seawater, as suggested by strontium, oxygen, and hydrogen isotopic data (Agrinier et al., 1993) and the low $^{40}Ar/^{36}Ar$ ratio (305) of the trapped argon.

^{4}He, ^{20}Ne, ^{40}Ar, and ^{36}Ar were measured in the orthopyroxenite vein rock Z31 by stepwise crushing and subsequent total fusion. Isotopic ratios show a well defined correlation with crushing step that indicates the presence of two different types or generations of inclusions, which were subjected to different degrees of contamination by atmosphere type noble gases. As inclusions were trapped before the main deformation of the peridotite complex (Kurat et al., 1993), argon with relatively low $^{40}Ar/^{36}Ar$ ratios ($\leq$1500) was trapped in the mantle, which requires an admixture of argon of atmospheric composition to the source region of the peridotites. Radiogenic isotopes (^{4}He, ^{40}Ar) are dominated by the mantle source, however, the $^{4}He/^{40}Ar$ ratio (~0.16) is much lower than expected from long term decay of radioactive parent nuclides U, Th, and K. Such low ratios, which have previously been observed also in mantle xenoliths, obviously reflect the indigenous peridotitic source and are most probably due to fractionation processes in the mantle.

1. INTRODUCTION

Zabargad Island in the Red Sea is regarded as the product of an asthenospheric diapir related to the break-up of the Nubian-Arabian plate and the opening of the Red Sea (e.g., Nicolas et al., 1985, 1987; Bonatti et al., 1986; Kurat et al., 1993). Thus, the Zabargad peridotites represent the continental upper mantle underneath the Red Sea. Because their uprising was relatively fast, they intruded the lower and upper crustal rocks while still being hot, causing considerable contact metamorphism. The quick ascent suppressed mineral facies adaptions to lower pressure. Therefore, Zabargad peridotites are astonishingly fresh, mainly of spinel peridotite facies, and mostly have unfractionated (primitive) bulk major and trace element contents (Bonatti et al., 1986; Kurat et al., 1993; Piccardo et al., 1993). However, some alterations can be traced in places and comprise depletions of some rocks in incompatible elements, metasomatic enrichments in such elements, formation of small amounts of amphibole and plagioclase with falling pressure, and metasomatic formation of amphiboles or clinopyroxenes or Al-spinel. Almost all of these alterations are related to tectonization of the originally protogranular peridotites. Last but not least, the Zabargad peridotite massives (there are three) characteristically have abundant vein rocks which are mostly monomineralic rocks like clinopyroxenites, orthopyroxenites, hornblendites, olivinites, and plagioclasites, and occasionally websterites. Such vein rocks are commonly interpreted as being cumulate rocks of magmatic activities in the upper mantle (e.g., Boudier and Nicolas, 1972; Cawthorn, 1975; Frey, 1980; Wilshire et al., 1991). Because a variety of mineralogical and chemical features is incompatible with such a genesis of monomineralic vein rocks, some other

*Present address: Institut für Planetologie, D-48149 Münster, Germany.

mechanisms have been proposed. Fairly popular is the idea of hydrothermal formation of such rocks (e.g., Bowen and Tuttle, 1949; Hess, 1969; Dungan and AvéLallement, 1977; Loomis and Gottschalk, 1981; Boudreau et al., 1986; Schiffries and Skinner, 1987). Extensive field studies, chemical bulk rock and mineral analyses, and studies of the fluid inclusions in the minerals of some vein rocks led Kurat et al. (1993) to the conclusion that most monomineralic vein rocks from Zabargad peridotites were formed by fluids consisting of CO_2 and N_2 and being devoid of water. By analogy, the cryptic and patent metasomatic alterations of some Zabargad peridotites have been considered to be the product of the very same fluids which formed the vein rocks.

In order to collect some additional arguments related to the genesis of monomineralic vein rocks, a study of the concentrations and the isotopic compositions of light noble gases was initiated. We also conducted ^{40}Ar-^{39}Ar analyses of neutron irradiated samples, which yield geochronological results, and moreover, are capable of detecting small-scale alterations of a rock by interaction with mantle-derived fluids (e.g., Turner et al., 1990). In order to separate the various noble gas components and to allow their relation to specific carriers, ^{40}Ar-^{39}Ar analyses were performed applying high resolution stepheating. It had first been demonstrated by Jessberger et al. (1974), that only then minor Ar components can safely be identified. Early work by Jessberger and Gentner (1972) showed that crushing techniques are highly valuable tools as well for further characterization of the noble gases in inclusions. We also applied stepwise crushing and subsequent total fusion as developed by Jambon et al. (1985). Our study attempts to provide insight into the complex history of the upper mantle, into the various possible sources of metasomatizing fluids, and into the complex fluid-rock interactions during tectonic uplift.

2. SAMPLE DESCRIPTIONS

Brief characterizations of the rocks based on previous studies are given below ordered by sample number. More detailed petrographic and mineralogical descriptions of Zabargad vein rocks can be found in Kurat et al. (1993) and electron microprobe measurements in Brandstätter et al. (1993).

Z13G: Plagioclasite

A vein of 2–3 cm width in spinel lherzolite from the main peridotite hill (MPH), Plagioclase (An 73) is very coarse-grained (cm) and shows deformed polysynthetic twin lamellae. Associated with plagioclase are porphyroclasts of olivine, clinopyroxene, orthopyroxene, and brown spinel. The latter is associated with some phlogopite and hornblende. Rare phases comprise pentlandite, ilmenite, and pyrite. The rare earth element (REE) content of Z13G is higher than that of the host lherzolite, which has an essentially flat CI chondrite-normalized REE pattern. Z13G REEs are slightly fractionated (La ~8 × CI, Lu ~3 × CI) with a small positive Eu anomaly.

Z28: Hornblendite

A pegmatoidal pocket of very coarse-grained amphibole (up to 10 cm in diameter) in harzburgite from the MPH. The hornblende is a magnesian pargasite with low TiO_2-content (0.37 wt%) and high Na_2O/K_2O (~8.5 by wt) and is associated with minor chlorite and carbonate. The REE content of the amphibole is high and slightly fractionated (La ~25 × CI, Lu ~10 × CI).

Z31: Orthopyroxenite

From a vein in harzburgite on central peridotite hill (CPH), it is a very coarse-grained pegmatoidal rock with grain sizes up to 10 cm. Orthopyroxenes are compositionally inhomogeneous (around En 90.3, Fs 9.0) and have exsolution lamellae of clinopyroxene in the cores but not near the grain surfaces. A few clinopyroxenes with exsolution lamellae of orthopyroxene are poikilitically included in orthopyroxene. Minor olivine and brown spinel are present. The REE content of the orthopyroxene is fairly high (La ~0.35 × CI, Lu ~2 × CI).

Z34: Spinel Plagioclase Lherzolite

The main rock type of the CPH is coarse-grained, porphyroclastic with some grain boundary recrystallizations. Large orthopyroxene has inclusions of olivine and tiny exsolution lamellae of clinopyroxene. Clinopyroxene has broad exsolution lamellae of orthopyroxene. Brown amphibole occurs interstitially. Olivine (Fo 90.7) porphyroclasts are kink-banded and occasionally include spongy orthopyroxene and small rounded spinel. Large holly-leaf spinel is green and surrounded by plagioclase. The chondrite normalized REE pattern is unfractionated, similar to other trace elements, and corresponds to the composition of the primitive upper mantle (Jagoutz et al., 1979).

Z102: Clinopyroxenite

This vein on CPH with clinopyroxene porphyroblasts up to 3 cm in equigranular matrix consists of clinopyroxene, a few orthopyroxene, vermicular intergranular spinel (brown) rimmed by plagioclase, and opaque phases. All pyroxenes have exsolution lamellae and are partially altered to amphibole of at least two different compositions (pargasite and hornblende). The REE content of the clinopyroxene is high (3–5 × CI), and the chondrite normalized concentration pattern almost flat.

Z103G: Clinopyroxenite

This vein is within spinel harzburgite (Z103H) on CPH. The rock is coarse-grained granular and contains scattered relics of olivine and orthopyroxene. Clinopyroxene has exsolution lamellae of spinel, orthopyroxene, and plagioclase. Primary clinopyroxene is rich in Al_2O_3 (6.7 wt%), and the neoblasts are Al_2O_3-poor (1.3 wt%). The REE abundances are high and fractionated relative to CI chondrites with La ~0.7 × CI and Lu ~7 × CI.

Z103H: Spinel Harzburgite

This is the host of clinopyroxenite Z103G. The rock exhibits a porphyroclastic texture with strongly deformed and kinked olivine and orthopyroxene porphyroclasts. Orthopyroxene has fine exsolution lamellae, and the spinel is brown. Portions of the rock contain strings of clinopyroxene porphyroblasts parallel to the foliation which have orthopyroxene and plagioclase exsolution lamellae. Interstitial spinel is rimmed by plagioclase. Some veins of olivine pyroxenites accompany the clinopyroxene strings and veins. The REE are depleted relative to upper mantle abundances and fractionated with Sm ~0.1 × CI and Lu ~1 × CI. The fractionation pattern does not comprise the light REE (La ~ Ce ~ Sm ~ 0.1 × CI), indicating some cryptic metasomatism.

3. EXPERIMENTAL PROCEDURES

Separates used for ^{40}Ar-^{39}Ar analysis were prepared by gently crushing large porphyroblasts of the main minerals and subsequent handpicking of grains between 200 and 2000 μm. Finally all separates were cleaned ultrasonically with diluted nitric acid, quartz distilled water, and ethanol. Separate Z28 was ~95% hornblende, containing some minor impurities, mainly chlorite. Z13G was ~90% plagioclase, with ~5% spinel and ~5% pyroxene. Separate Z102 consisted of ~50% clinopyroxene and ~50% (nonseparable) orthopyroxene, which were partially amphibolized and serpentinized. Z103G was ~85% clinopyroxene, ~10% orthopyroxene and <5% spinel.

^{40}Ar-^{39}Ar analysis followed standard procedures given by Jessberger et al. (1980). The samples were wrapped in high-purity aluminum foil (99.999%) and stacked in a quartz ampoule. Cadmium shielding was used to prevent irradiation damage. Specimens Z28#2, Z13G#2, Z102, and Z103G were exposed to a fast neutron dose of approximately 2×10^{18} neutrons$_f$/cm^2 in the BR2-reactor in Mol/Belgium. The corresponding J-value was 0.01200 ± 0.00003 and the relative flux variation along the 3 cm long irradiation capsule was 0.15%, as monitored by NL25 hornblende standards (Schaeffer and Schaeffer, 1977). Correction factors for interfering isotopes determined by a CaF_2 and the NL25 monitors were $(^{36}Ar/^{37}Ar)_{Ca} = (3.59 \pm 0.10) \times 10^{-4}$, $(^{38}Ar/^{37}Ar)_{Ca} = (5.58 \pm 0.20) \times 10^{-5}$, $(^{39}Ar/^{37}Ar)_{Ca} = (9.07 \pm 0.02) \times 10^{-4}$, $(^{38}Ar/^{39}Ar)_K = (1.708 \pm 0.050) \times 10^{-2}$. The samples were heated to temperatures from 300°C to 1550°C (60 min) using a low blank furnace (Staudacher et al., 1978) with ^{40}Ar blank values varying from 0.013 to 0.025 at 300°C and 0.069 to 0.138 at 1550°C (in units of 10^{-8} ccSTP).

Samples Z28#1 and Z13G#1 were irradiated in the GKSS-reactor in Geesthacht, Germany, with a J-value of $(2.916 \pm 0.027) \times 10^{-4}$. Correction factors as determined by a CaF_2 and HD-B1 monitors (Fuhrmann et al., 1987) were: $(^{36}Ar/^{37}Ar)_{Ca} = (5.00 \pm 0.11) \times 10^{-4}$, $(^{38}Ar/^{37}Ar)_{Ca} = (1.811 \pm 0.004) \times 10^{-3}$, $(^{39}Ar/^{37}Ar)_{Ca} = (9.03 \pm 0.04) \times 10^{-4}$, $(^{38}Ar/^{39}Ar)_K = (2.0405 \pm 0.0015) \times 10^{-2}$. Heating temperatures ranged from 400°C to 1600°C (15 min) using an induction-heated furnace with ^{40}Ar blank values varying from 0.0125 to 0.0130 at 400°C and from 0.320 to 0.423 at 1600°C (in units of 10^{-8} ccSTP).

For both irradiations neutron-produced ^{40}Ar was corrected with $(^{40}Ar/^{39}Ar)_K = (1.23 \pm 0.24) \times 10^{-2}$ (Brereton, 1970) and $(^{40}Ar/^{37}Ar) = (3 \pm 3) \times 10^{-3}$ (Turner, 1971). After heating, the released gas was purified by SAES and Ti-getter and analyzed by a sector field magnet mass spectrometer (CH5 Varian MAT). Mass discrimination and sensitivity were determined by daily measurements of a pipetted Ar-volume of 19.54×10^{-8} ccSTP ^{40}Ar. Sensitivity and mass discrimination also vary systematically with the absolute amount of the measured gas, an effect widely not taken into account. For example, a variation of the total gas amount by 3 orders of magnitude causes sensitivity and mass discrimination differences of 20 and 4%, respectively. These variations were monitored by measurements of divided and multiple amounts of the pipetted volume. Usually the absolute gas amounts are the major source of uncertainty for K, Ca, and Cl concentrations. After applying this procedure, the comparison with two samples on which K was measured for K-Ar dating showed an agreement of better than 0.5%. Therefore, we consider K and Ca contents to have an uncertainty of 2%. Conversion factors usually have as small uncertainties as the J-values and were determined from the NL25 hornblende monitor (3070 ppm K and 8.04% Ca) to $^{39}Ar_K/K = 8400 \pm 21$ [10^{-8} ccSTP/g] and $^{37}Ar_{Ca}/Ca = 4290 \pm 11$ [10^{-8} ccSTP/g]. For the Geesthacht irradiation, the K conversion factor of $^{39}Ar_K/K = 204 \pm 1.9$ [10^{-8} ccSTP/g] was determined via the HD-B1 monitor (7.987% K). The Ca conversion factor of $^{37}Ar_{Ca}/Ca = 106 \pm 0.1$ [10^{-8} ccSTP/g] was derived from the CaF_2 standard (51.3% Ca). The Cl conversion factor in Mol of $^{38}Ar_{Cl}/Cl = 2110$ [10^{-8} ccSTP/g] was determined in the course of a previous irradiation for a J-value of 0.01 (Jessberger et al., 1980) with neutron-irradiated Pyrex glass (750 ppm Cl). As adjusting to a different J-value assumes the same ratio of thermal and fast neutrons for different irradiations (although in the same reactor), we estimate a larger uncertainty (15%) for Cl than for K and Ca. For Geesthacht, the same value was used. Although the Cl results for Geesthacht should be taken with caution due to the difficult uncertainty estimate, good agreement can be observed between the Cl values of the two different irradiations (i.e., for Z28 in Table 1). Decay constants for age calculations are those recommended by Steiger and Jäger (1977). Tables with corrected argon isotope concentrations for the individual samples are given in the Appendix.

Helium, neon, and argon analyses of nonirradiated samples followed procedures described by Weber et al. (1983) and were done on a simple focussing Nier type mass spectrometer, built at the Max-Planck-Institut für Chemie, Mainz. Argon was adsorbed on charcoal at the temperature of boiling nitrogen, while He and Ne were admitted to the mass spectrometer. Whole rock chips (wrapped in high purity iron foil) of Z34, Z103G, Z103H, and Z31 were analyzed by total fusion in one step. Furthermore, an unwrapped whole rock chip of Z31 was crushed at room temperature by dropping a Ta slug onto the sample lying on a heavy Mo insert in the Ta tube. Subsequently two aliquots of the sample were heated (further experimental details in Jambon et al., 1985). Spectrometer sensitivity was checked periodically against a gas standard, of which the reproducibility was within 2%.

Mineral analysis were carried out using an ARL-SEMQ electron microprobe and standard correction procedures implemented at the Max-Planck-Institut für Kernphysik in Heidelberg.

4. RESULTS AND DISCUSSION

4.1. ^{40}Ar-^{39}Ar chronology

We analyzed duplicate samples of hornblende from Z28 and plagioclase from Z13G. Both were separated from the host vein rock, but the crystals were not crushed and homogenized to avoid loss of indigenous Ar and contamination by atmospheric Ar. The larger samples (designated #1) allowed fine resolution of the radiogenic component and the main ^{39}Ar-release, while smaller samples (#2) were analyzed in equidistant temperature steps resulting in a better resolution of the trapped and excess argon components. Figure 1 shows the ^{40}Ar-^{39}Ar age spectra of the Z28-hornblende and the Z13G-plagioclase separates. Z28-separates yielded ages around 20 Ma over 90% of the ^{39}Ar release, close to a Pb-Pb zircon age of 18.4 ± 1.0 Ma, that has been interpreted as the time of intrusion by Oberli et al. (1987). The first few percent of the ^{39}Ar-release are dominated by excess argon, most clearly seen in the highly resolved low temperature part of spectrum #2. Plagioclase exhibits a saddle-shaped age spectrum, pointing to the presence of excess argon (Lanphere and Dalrymple, 1976; Harrison and McDougall, 1981), with ages up to 700 Ma; only the me-

Table 1. Analytical data obtained by ^{40}Ar-^{39}Ar stepheating dating of Zabargad vein rock separates. Uncertainties of K and Ca concentrations are 2% and are compared to data obtained by X-ray fluorescence (XRFA), neutron activation (INAA) analysis (Kurat et al., 1993), and electron microprobe analysis (EMPA) of the main minerals (this work and Brandstätter et al., 1993).

Samples[a]	Hornblende Z28 #1/#2	Plagioclase Z13G #1/#2	Clinopyroxene Z102	Clinopyroxene Z103G
^{40}Ar-^{39}Ar age [Ma]	18.7 ± 1.3[b]	<16.7 ± 0.9[b]	—	—
K-Ar age [Ma]	22.3/34.1	269/207	2035	3098
^{36}Ar [10^{-8} cc/g]	0.380/0.407	0.085/0.204	0.333	0.040
$^{40}Ar_{rad}$ [10^{-8} cc/g]	8.0/5.8	6.3/5.1	1.2	0.2
$^{40}Ar_{atm}$[c] [10^{-8} cc/g]	112.3/120.2	25.1/60.2	98.2	11.7
$^{40}Ar_{excess}$ [10^{-8} cc/g]	3.8/8.2	98.7/60.9	243.6	97.6
$^{40}Ar_{atm}$ [%]	89/88.2	19.3/47.7	28.6	10.7
$^{40}Ar_{excess}$ [%]	3.0/6.0	75.8/48.3	71	89.1
$^{40}Ar/^{36}Ar_{excess}$	305.3 ± 2.7	<7000	<2000	<8000
K [ppm]	1597/1222	933/727	168	31
$K_{EMPA/INAA}$ [ppm]	2074/(1850[d])	581/1430	80 ± 45[e]/275	<84[e]/51/(210[d])
ΔK_{EMPA}[f] [ppm]	166–11780	166–664		
Ca [%]	8.85/5.96	8.77/6.58	8.59	8.39
$Ca_{EMPA/XRFA}$ [%]	8.79/12.63	10.2/8.70	13.4–17.3; 16.2[e]/8.61	12.4–16.8; 17.0[e]/12.39
Ca_{EMPA}[e] [%]			16.2	17.0
ΔCa_{EMPA}[f] [%]	7.3–8.9	4.1–12.5	12.4–17.3	12.4–17.3
Cl [ppm]	3828/4161	8/51	971	275
Cl_{INAA} [ppm]	(5000[d])	180	1240	560 (1050[d])
Cl_{EMPA}[e] [ppm]	—	—	220 ± 45	<200
Sample weight [mg]	244.1/44.3	307.6/50.1	125.0	134.2

[a] Age determinations were carried out on mineral separates (main minerals) of the rocks.

[b] Uncertainties quoted for the plateau age are 1σ errors and do not contain the error of the laboratory standards, which were used for calibration. To compare the data with ^{40}Ar-^{39}Ar ages of laboratories using different monitor minerals, an additional error of 0.4 Ma has to be added.

[c] All ^{36}Ar and the 295.5-fold amount of ^{40}Ar is designated as "atmospheric argon", but is actually an upper limit, because it could be excess argon exclusively.

[d] Determined on mineral separates Z28C, Z103C.

[e] Best EMPA estimates for clinopyroxene obtained in the course of this work.

[f] Ranges determined by electron microprobe on minerals of all rock types.

dium release yields apparent ages close to 20 Ma. Considering the extended age scale (Fig. 2b), the better resolved main release of Z28#1 displays stepwise decreasing ages, the high temperature release even with ages below the Pb-Pb datum. However, the isochrone (Fig. 2a) shows a good correlation of the data points of the main release pointing to a trapped $^{40}Ar/^{36}Ar$ ratio of 305.3 ± 2.7, different from the atmospheric ratio. Correcting the spectrum with this ratio (Fig. 2b) yields a plateau consisting of four fractions comprising 75% of the ^{39}Ar release with an age of 18.7 ± 1.3 Ma, in agreement with the above quoted Pb-Pb age.

As we did not use aliquots sensu stricto, some minor differences between samples #1 and #2 are not surprising, e.g., in the low temperature K/Ca and age spectrum of Z13G and part of the Z28 age spectrum. These differences could be due to different abundances of minor phases in Z13G and varying excess argon concentrations in Z28. The last six temperature fractions of the Z28 spectrum drop in age, which is interpreted as an artefact by ^{39}Ar recoil (Turner and Cadogan, 1974; Huneke and Smith, 1976). At first sight this seems improbable, as the hornblende grain size is in the range of 100 μm or mm. In order to account for ages lower than the plateau value of 18 Ma, 12% of the total amount of ^{39}Ar would have to be redistributed into a K-poor phase. Such a large fraction is usually lost only by grains with a large surface/volume ratio: if the grain size is calculated for spherical grains from the ^{39}Ar fraction (Trieloff, 1990; Trieloff et al., 1994) the resulting grain radius is ~1 μm. A possible explanation is the occurrence of μm-sized impurities or exsolution features as observed, e.g., by Harrison and Fitz Gerald (1986). These authors observed K-poor cummingtonite exsolution lamellae within a metamorphic amphibole at the micrometer scale, but with different domain sizes ranging from 4 nm, only visible with TEM-techniques, to 20 μm. The constant K/Ca-spectrum of Z28 (Fig. 1) would imply that the receptor phase is depleted in Ca in the same degree as K, which is, e.g., the case for cummingtonite. This mineral, however, has to be quite Ar-retentive to account for the effects, which is not proven yet. Onstott and Peacock (1987) observed alteration zones of fibrous phyllosilicates of 0.1 up to 2 μm width. Our own SEM investigations did not reveal such minor phases, although this may be due to the limited SEM-resolution. However, Z28 Ca concentrations determined by electron microprobe spot analyses (Brandstätter et al., 1993) and from Ca-derived ^{37}Ar are consistent, allowing only minor amounts of Ca-poor alteration features. Another possibility is the occurrence of two lattice sites with different retentivity for the Ar atoms within hornblende. Part of the ^{39}Ar could be transferred to more retentive sites by ^{39}Ar recoil and released at higher temperatures. In this case no μm-sized phases are necessary, however, up to now, there has been no evidence for lattice sites of differing retentivity, so the last possibility remains speculative.

Previous ^{40}Ar-^{39}Ar dating attempts (Villa, 1990) of Zabar-

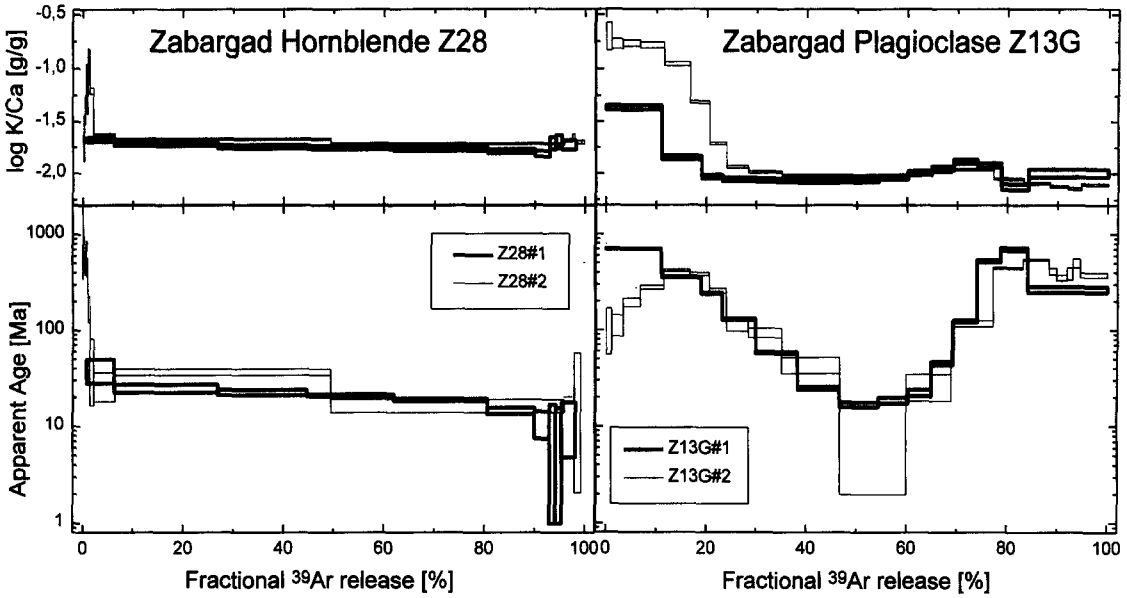

Fig. 1. Age spectra and K/Ca spectra of the hornblende and plagioclase separates. Z28#1 shows a nearly flat (plateau-like) age spectrum, while Z13G exhibits a typical saddle shaped age spectrum, indicative of excess argon, which is not due to in situ K-decay.

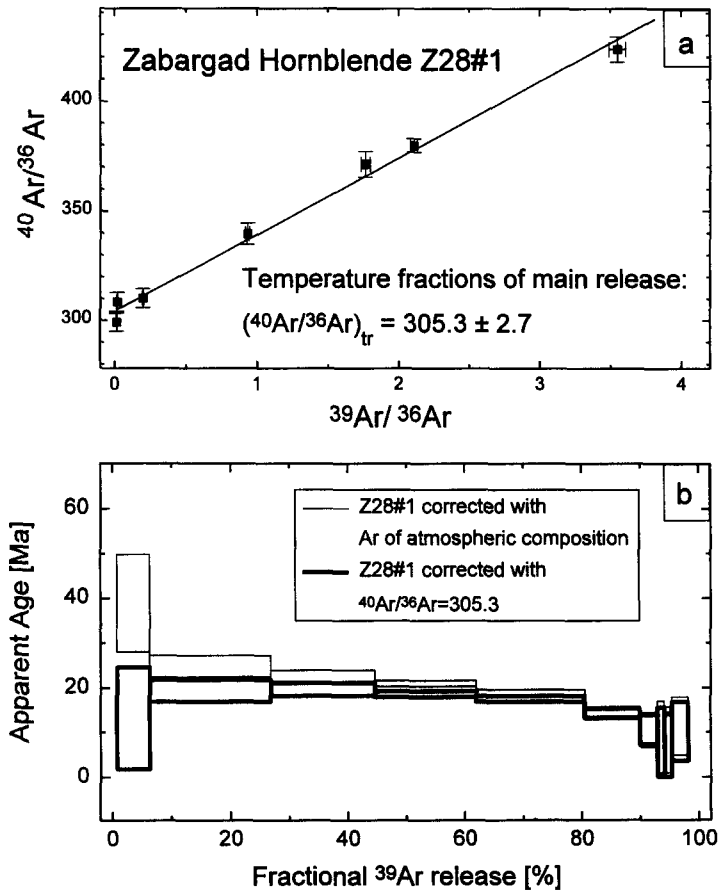

Fig. 2. (a) Isochrone of Z28 hornblende: the main release data are linearly correlated pointing to a trapped $^{40}Ar/^{36}Ar$ ratio of 305.3 ± 2.7. Correction of the age spectrum with this value instead of the atmospheric ratio of 295.5 results in a plateau of 18.7 ± 1.3 Ma, as shown in (b)

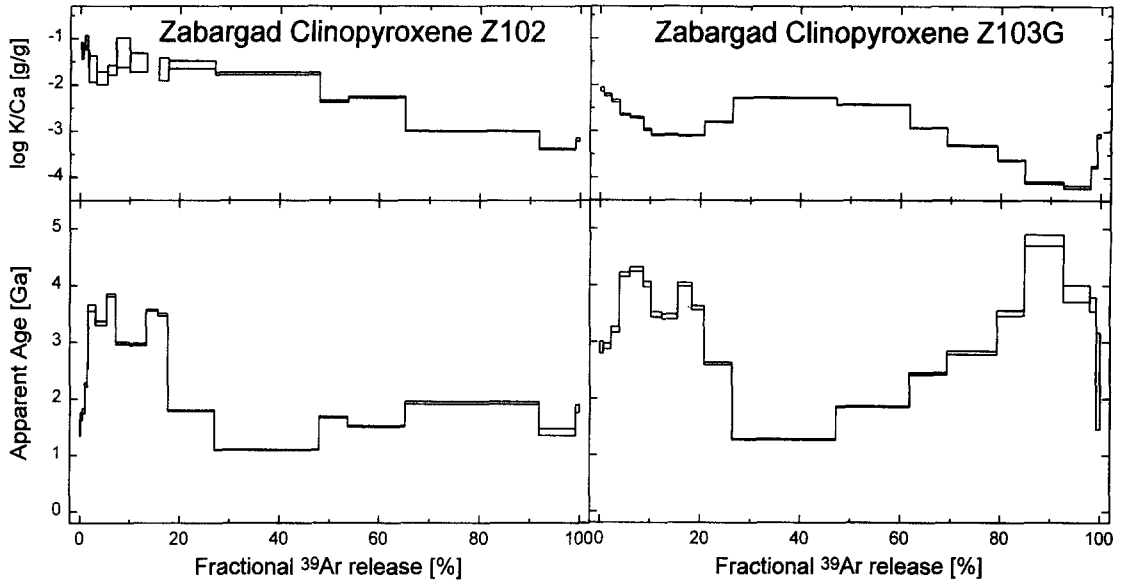

Fig. 3. K/Ca- and age spectra of the clinopyroxene separates Z102 and Z103G. Variable ages between 1 and 5 Ga indicate decoupling of parent and daughter nuclide of the K-^{40}Ar system. Thus, most of the ^{40}Ar is trapped.

gad amphiboles failed, because the samples were strongly contaminated with excess argon. Another reason probably was, that the sharp main gas release was not measured with sufficient resolution (50°C steps in comparison to 10°C steps of Z28#1), as was also the case for our sample Z28#2 that did not yield useful isochron data.

For plagioclase Z13G#1, the age value of the fraction lowest in age is 16.7 ± 0.9 Ma and serves as an upper limit for the last time of resetting (Jessberger, 1977). As this is not significantly younger than the hornblende, the age data are consistent with a fast uplift history, because a slow uplift probably would have caused a resolvably younger age for the less retentive plagioclase. On the other hand, a slow uplift cannot definitely be excluded by these chronological data, as the 16.7 Ma old fraction might be also contaminated with excess argon. The K/Ca spectra of Z28 and Z13G show plateaux with K/Ca ratios consistent with electron microprobe measurements on these minerals (Brandstätter et al., 1993), except for the high K/Ca ratios in the beginning of the Z13G spectrum, which is a hint to a further K-bearing phase.

Clinopyroxenes Z102 and Z103G (Fig. 3) exhibit varying apparent ages between 1 and 5 Ga. K/Ca spectra drop to very low ratios at the end of the ^{39}Ar release, a feature commonly observed for pyroxene separates, which will be explained later. Using the measured K concentrations, the percentage of radiogenic ^{40}Ar decayed in situ since 18 Ma can be calculated to be very low, 0.3 and 0.2%, respectively. If the peridotite complex was intruded 18 Ma ago into the crust, most ^{40}Ar must have originated from the upper mantle. ^{40}Ar/^{36}Ar ratios of the clinopyroxenites range up to 8000, which is in agreement with the observation, that (even zero age) mantle derived rocks are characterised by high ^{40}Ar/^{36}Ar ratios (Sarda et al., 1985; Jambon et al., 1985; Staudacher et al., 1989; Poreda and Farley, 1992; Matsuda and Marty, 1995). In principle, ^{40}Ar could be trapped or could have originated from in situ K decay within the upper mantle. The decoupling of K and ^{40}Ar visible in the age spectra rather suggests that it is trapped, however, we will be able to draw more definite conclusions after identification of the Ar carriers.

Table 1 summarizes the analytical data obtained by the ^{40}Ar-^{39}Ar technique. For comparison, K, Ca, and Cl measurements by INAA, XRFA, and electron microprobe are also included (Kurat et al., 1993; Brandstätter et al., 1993). Chemical compositions agree by and large; differences, where significant, are most probably due to sample inhomogeneities.

4.2. Electron Microprobe Analyses

Clinopyroxenite Z102 consists mainly of clinopyroxene with ~10–100 μm wide exsolution lamellae of orthopyroxene. The major parts of the thin section show almost no or few alterations (Fig. 4a). Other areas exhibit stronger signs of alteration with numerous serpentine clasts, amphibolized clinopyroxene, and inclusions down to the μm range (Fig. 4b,c). Electron microprobe analysis (EMPA) were made for Z102 clinopyroxene, orthopyroxene, amphibole, and serpentine and are shown in Table 2a. For clinopyroxenite Z103G (Fig. 4d), results for clinopyroxene, amphibole, plagioclase, and olivine are shown in Table 2b.

4.3. Identification of Major and Minor Carrier Phases of Trapped Argon Components

The high resolution degassing pattern of the hornblendite and clinopyroxenite samples (Figs. 5,6) show the fractional gas release with increasing degassing temperature. As Ca, K, and Cl are measured as argon isotopes as well, their degassing characteristics can be used to constrain the carrier phases responsible for ^{40}Ar and ^{36}Ar release peaks (or reservoirs) at different temperatures. This way it is possible to

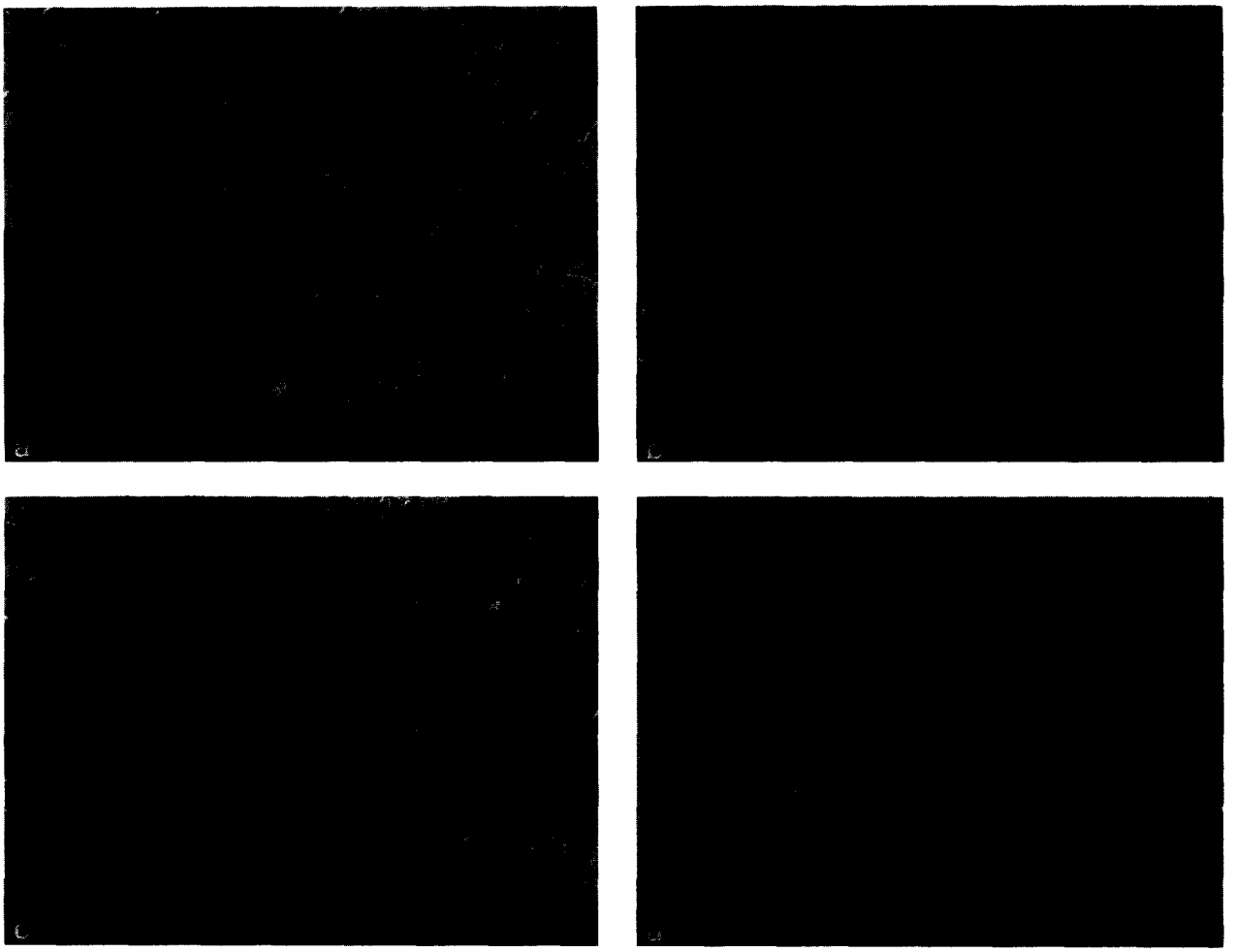

Fig. 4. SEM micrographs showing (a) (10–100 μm wide exsolution lamellae of clinopyroxene (light grey) and orthopyroxene (dark grey) of clinopyroxenite Z102; almost no alterations are visible in this part of the section. (b,c) stronger altered parts with serpentinized orthopyroxene (black) and amphibolized clinopyroxene (medium grey features in light grey clinopyroxene lamellae); inclusions down to the micron range are visible; direction of pyroxene lamellae: from upper left to lower right. (d) part of a section of clinopyroxenite Z103G with clinopyroxene (light grey), amphibole (medium grey), olivine, and plagioclase (dark grey).

identify one or more noble gas hosts in order to check, e.g., whether the main phase or a minor accessory, nonseparable phase contain the major fraction of the trapped argon. Moreover, if $^{40}Ar/^{36}Ar$ ratios associated with different phases are different in turn, they give further clues to the origin and individual history of the carrier phases.

4.3.1. Hornblendite Z28

Z28 (Fig. 5) shows a typical sharp peak at 1000–1100°C which is characteristic for amphibole (Onstott and Peacock, 1987; Hanson et al., 1975; Berger, 1975), although in a few cases low temperature peaks are observed (Harrison and McDougall, 1981; Berger, 1975). In the case of Z28, the isotopes ^{39}Ar and ^{37}Ar derived from the lattice elements K and Ca degas simultaneously, as well as K correlated radiogenic ^{40}Ar (Fig. 5 a,b). This results in a constant K/Ca spectrum ($\approx$ 0.02) and a nearly plateau age spectrum for Z28#1 (Fig. 1). Ages exceeding the intrusion age of 18 Ma in the low temperature fractions of Z28#2 have their counterpart as small low temperature peaks of excess ^{40}Ar at 400–900°C (Fig. 5b). Trapped ^{36}Ar of Z28#2 (Fig. 5c) degasses also at lower temperatures, correlated with excess argon, with varying $^{40}Ar_{exc}/^{36}Ar$ ratios of 300–330. Recent investigations of hydrothermally altered pseudotachylites revealed the association of excess argon released at 500–700°C and calcite (Trieloff et al., 1994). Thus, at least part of the low temperature excess component could be associated with carbonates that have also been detected within Z28 hornblende by SEM. However, the excess component of Z28#1 identified via the isochrone (Fig. 2a) with $(^{40}Ar/^{36}Ar)_{exc}$ = 305.3 is trapped within the main reservoir, that means within the amphibole.

4.3.2. Plagioclasite Z13G

The degassing pattern of plagioclasite Z13G (not plotted here) is rather complex: a couple of features have to be explained; some of them, especially the excess argon components, cannot be definitely tied to a specific mineralogical

Table 2a. Chemical composition of clinopyroxene (cpx), orthopyroxene (opx), amphibole (amph), and serpentine (serp) in Z102 as determined by electron microprobe analysis (EMPA)[a].

Title	SiO_2	TiO_2	Al_2O_3	Cr_2O_3	V_2O_3	FeO*	MnO	MgO	NiO	CaO	K_2O	Na_2O	Cl	Total	Cl=O	Total
monitor	55.0	b.d.	b.d.	b.d.	b.d.	0.04	b.d.	18.4	b.d.	26.1	0.00	b.d.	0.03	99.60	0.007	99.59
cpx 2a-5	54.6	0.03	0.62	0.30	0.03	1.91	0.10	17.8	0.02	24.4	0.01	0.21	0.02	100.04	0.005	100.03
cpx 2b-17	52.8	b.d.	1.77	1.24	0.04	2.93	0.10	16.2	0.02	23.9	0.01	0.43	0.02	99.44	0.005	99.43
cpx 2c-26	52.9	0.26	5.06	1.15	0.04	2.39	0.10	14.7	0.06	21.3	0.00	1.61	0.02	99.59	0.005	99.58
cpx 2c-27	52.4	0.24	5.10	1.12	0.07	2.32	0.11	14.5	0.07	21.4	0.01	1.59	0.02	98.95	0.005	98.94
cpx 2c-31	52.3	0.26	5.31	1.27	0.07	2.45	0.09	14.5	0.04	22.2	0.01	1.60	0.03	100.05	0.007	100.04
opx 2a-1	53.2	b.d.	3.71	0.67	b.d.	6.75	0.15	34.1	0.06	0.46	0.00	b.d.	0.01	99.14	0.002	99.14
opx 2b-14	53.7	b.d.	3.31	0.57	b.d.	8.09	0.17	31.6	0.08	0.52	0.00	0.03	0.01	98.11	0.002	98.11
opx 2b-15	54.1	0.02	3.56	0.60	b.d.	6.49	0.13	33.1	0.08	0.59	0.00	0.02	0.03	98.68	0.007	98.67
opx 2c-23	54.6	0.03	4.03	0.61	b.d.	6.51	0.17	32.1	0.08	0.56	0.00	b.d.	0.01	98.61	0.002	98.61
amph 2a-3	49.5	0.11	7.05	1.08	b.d.	4.11	0.07	19.9	0.05	12.9	0.20	1.26	0.34	96.56	0.077	96.48
amph 2a-4	48.5	0.30	7.83	1.48	0.07	3.89	0.04	19.3	0.07	12.8	0.19	1.42	0.49	96.37	0.111	96.26
amph 2b-18	46.3	0.38	8.79	1.42	0.09	5.63	0.09	18.7	0.06	12.4	0.23	1.48	0.41	96.03	0.093	95.94
serp 2a-6	41.4	0.09	0.24	b.d.	b.d.	3.32	0.09	35.1	b.d.	0.14	0.03	0.07	0.54	80.96	0.122	80.84
serp 2a-8	42.5	b.d.	0.10	0.02	b.d.	2.37	0.07	30.5	b.d.	0.23	0.17	0.16	0.27	76.38	0.061	76.32
serp 2a-12	38.7	b.d.	3.01	0.30	0.06	3.33	0.07	32.8	b.d.	0.15	0.05	0.05	0.69	79.17	0.156	79.01
serp 2b-13	39.3	b.d.	0.37	b.d.	b.d.	3.42	0.08	35.1	b.d.	0.14	0.03	0.04	0.54	78.96	0.122	78.84

[a] Values below 0.02% are given as b.d. (below detection), except for K and Cl, in order to facilitate the calculations of average values.

phase. However, the at least partial open-system behaviour of the K-Ar system until intrusion shows that this rock may have lost its mantle derived noble gases. Therefore, we will exclude it from the discussion of mantle noble gases which follows later.

4.3.3. Clinopyroxenites

In general it can be found for terrestrial and extraterrestrial pyroxene separates, that Ca correlated ^{37}Ar is released at very high temperatures (1300–1400°C); K correlated ^{39}Ar is released between 700 and 1100°C (for lunar pyroxene see Turner et al., 1972; Jessberger et al., 1974; Stettler et al., 1974; Horn et al., 1975; for meteoritic pyroxene see Flohs, 1979 and Trieloff, 1990; for terrestrial pyroxene see Lanphere and Dalrymple, 1976; Harrison and McDougall, 1981; Trieloff, 1993). In no case does the main ^{39}Ar release occur at similarly high temperatures as for ^{37}Ar. This observation leaves the only viable explanation, that the main K-bearing

Table 2b. Chemical composition of clinopyroxene (cpx), amphibole (amph), plagioclase (plag) and olivine (olv) in Z103G as determined by electron microprobe analysis[a].

Title	SiO_2	TiO_2	Al_2O_3	Cr_2O_3	V_2O_3	FeO*	MnO	MgO	NiO	CaO	K_2O	Na_2O	Cl	Total	Cl=O	Total
diopsid mon.-1	56.4	b.d.	b.d.	b.d.	b.d.	0.03	b.d.	17.6	b.d.	25.3	0.00	b.d.	0.00	99.29	0.000	99.29
monitor-2	57.5	b.d.	b.d.	0.03	b.d.	0.02	b.d.	17.8	b.d.	25.7	0.01	b.d.	0.03	101.06	0.007	101.05
monitor-3	56.5	b.d.	0.03	b.d.	0.05	0.03	0.03	17.2	b.d.	25.6	0.01	b.d.	0.02	99.43	0.005	99.42
cpx-1	53.2	0.04	1.43	0.75	0.11	2.25	0.09	16.7	0.05	23.4	0.00	0.44	0.00	98.47	0.000	98.47
cpx-2	54.2	0.03	1.51	0.73	0.14	2.06	0.08	15.0	b.d.	24.3	0.00	0.44	0.02	99.47	0.005	99.46
cpx-3	53.8	0.04	2.03	0.85	0.16	2.35	0.07	15.6	0.04	23.8	0.01	0.43	0.01	99.18	0.002	99.18
amph-4	41.5	0.16	14.8	0.57	0.18	6.38	0.07	12.9	0.11	13.6	0.06	2.78	0.18	93.27	0.041	93.23
amph-5	40.9	0.19	14.5	0.77	0.21	5.95	0.04	13.7	0.09	12.6	0.06	2.84	0.21	91.97	0.047	91.92
amph-17	44.5	0.13	13.3	0.75	0.18	5.76	0.04	13.1	0.09	13.9	0.07	2.41	0.19	94.24	0.043	94.20
amph-26	44.4	0.32	11.5	1.14	0.23	5.36	0.08	14.9	0.07	13.0	0.06	2.57	0.17	93.88	0.038	93.84
plag-6	43.8	b.d.	35.5	b.d.	b.d.	0.09	b.d.	b.d.	b.d.	19.6	0.01	0.62	0.00	99.66	0.000	99.66
plag-7	48.5	b.d.	31.6	b.d.	b.d.	0.40	b.d.	0.10	b.d.	15.2	0.00	2.43	0.03	98.33	0.007	98.32
plag-8	50.8	b.d.	33.0	b.d.	0.03	0.21	b.d.	b.d.	0.02	15.2	0.00	2.61	0.01	102.90	0.002	102.90
plag-19	49.7	b.d.	30.9	b.d.	b.d.	0.11	0.04	b.d.	b.d.	14.7	0.00	2.53	0.01	98.07	0.002	98.07
plag-20	48.4	b.d.	33.2	b.d.	b.d.	0.11	b.d.	b.d.	b.d.	16.7	0.00	2.04	0.00	100.45	0.000	100.45
plag-22	50.1	b.d.	32.1	b.d.	b.d.	0.16	b.d.	0.03	b.d.	15.2	0.00	2.50	0.01	100.07	0.002	100.07
plag-23	49.6	b.d.	33.7	b.d.	b.d.	0.11	b.d.	b.d.	b.d.	15.9	0.00	2.23	0.00	101.41	0.000	101.41
olv monitor-1	41.6	0.04	b.d.	b.d.	b.d.	7.16	0.12	50.89	0.49	b.d.	0.01	b.d.	0.01	100.34	0.002	100.34
olv-10	41.8	b.d.	0.03	0.02	0.02	9.88	0.21	47.7	0.49	0.09	0.00	b.d.	0.01	100.21	0.002	100.21
olv-11	41.5	b.d.	0.04	b.d.	b.d.	9.46	0.23	47.9	0.44	0.12	0.00	b.d.	0.00	99.68	0.000	99.68
olv-24a	41.6	b.d.	b.d.	b.d.	0.03	9.60	0.23	48.3	0.44	0.10	0.00	b.d.	0.00	100.30	0.000	100.30
olv-24b	41.8	b.d.	0.04	b.d.	b.d.	9.60	0.20	48.0	0.49	0.10	0.00	0.02	0.01	100.30	0.002	100.30
olv-24c	40.9	0.04	b.d.	0.02	b.d.	9.62	0.23	48.4	0.48	0.08	0.00	b.d.	0.00	99.72	0.000	99.72
olv-24d	41.7	0.02	b.d.	0.03	b.d.	9.31	0.21	47.7	0.40	0.08	0.00	b.d.	0.00	99.44	0.000	99.44
olv-24e	42.3	b.d.	b.d.	0.04	b.d.	9.47	0.20	48.3	0.45	0.15	0.00	b.d.	0.02	100.88	0.005	100.87

[a] Values below 0.02% are given as b.d. (below detection), except for K and Cl, in order to facilitate the calculations of average values.

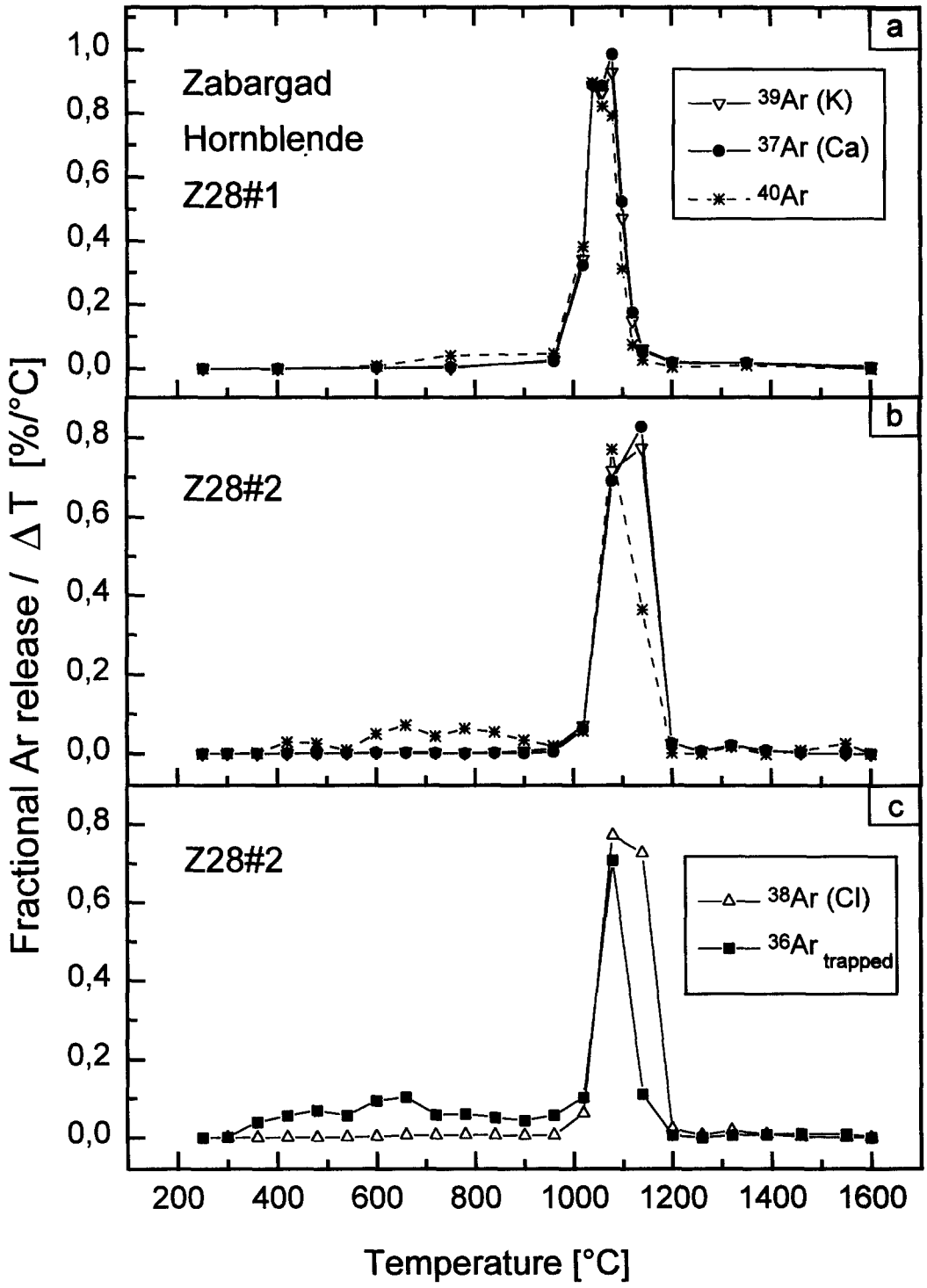

Fig. 5. Degassing pattern of argon isotopes of Z28 hornblende. Note sharpness of the main peak for all isotopes. A minor low temperature reservoir for a trapped Ar component could probably be associated with carbonates.

phases within pyroxene separates are impurities, for example, minor phases such as plagioclase, amphibole, or phlogopite, rather than K in the pyroxene lattice. This is also valid for Z103G (Fig. 6), which follows the general feature outlined above. However, in the case of Z102 K-derived ^{39}Ar degasses also at 1300–1400°C. As to our knowledge, such a pattern has not yet been observed, in particular throughout the work quoted above, which represents a quite complete survey of ^{40}Ar-^{39}Ar dating of pyroxene separates. From the K/Ca ratio of Z102 derived from EMPA and argon isotopes, we calculate that about 50% of the K released in the high temperature (pyroxene) reservoir (~80 ppm) could reside

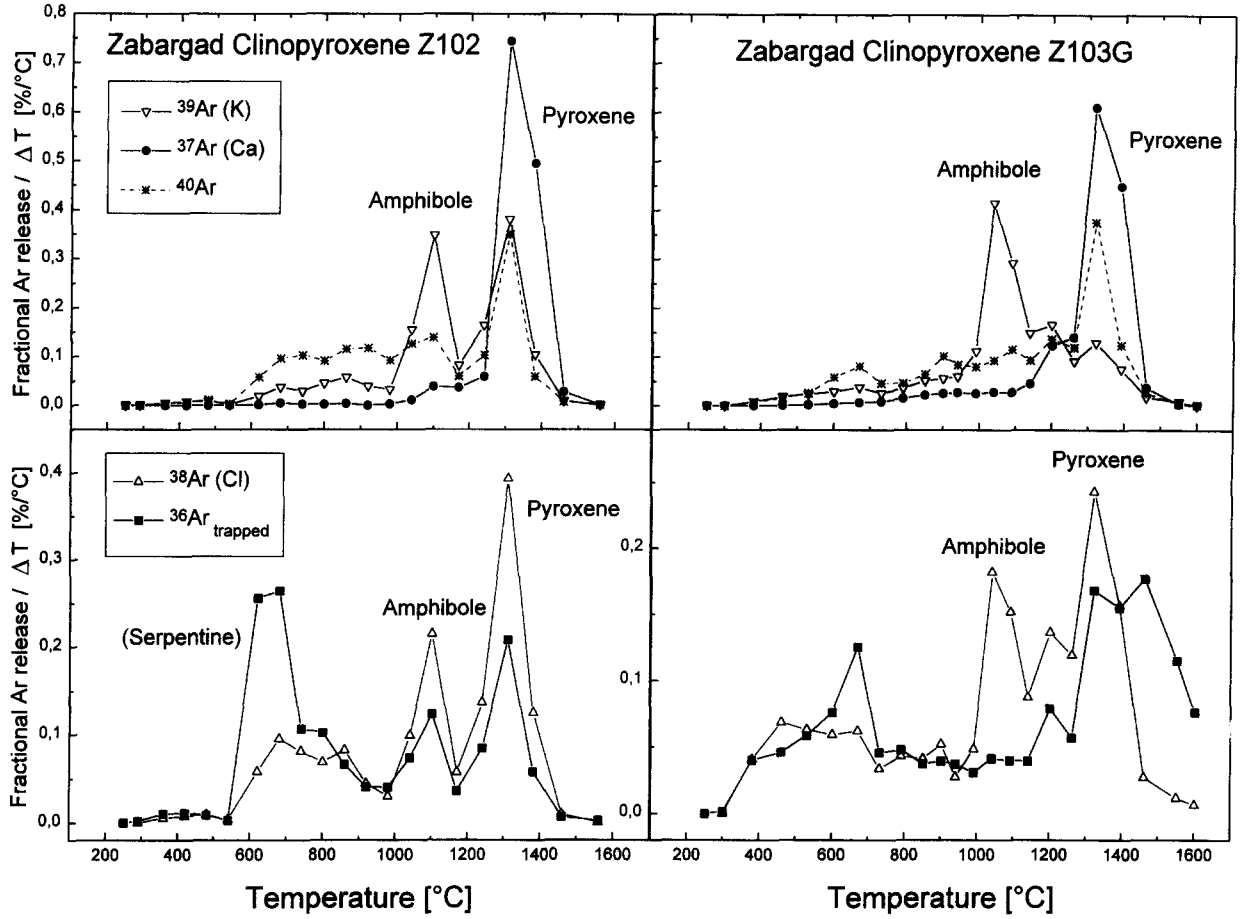

Fig. 6. Degassing pattern of argon isotopes of Z102 and Z103G clinopyroxene separates. Pyroxene and amphibole gas release regimes are indicated.

in the pyroxene lattice, though large EMPA uncertainties. The remaining 50% could be due to accessory minerals or inclusions which are completely encapsuled by the exceptionally large pyroxene crystals. The compatibility of K in clinopyroxene under high pressure has been supported by recent experiments of Harlow (1997) and could independently testify the high pressure (mantle) environment during clinopyroxene genesis. On the other hand, the K concentration (calculated from ^{39}Ar) in the clinopyroxene reservoir of Z103G is rather low (6.1 ppm), but K uptake under high pressure may be related to specific dircumstances (Harlow, 1997).

The medium temperature reservoirs releasing ^{39}Ar at 1000–1100°C are not encapsuled K-phases and very probable amphiboles. This is inferred from the degassing temperature (see Z28 amphibole) and from the K/Ca ratios (log K/Ca = −1.74 and −2.27 for the largest fractions of Z102 (1100°C) and Z103G (1040°C), respectively): these are consistent with our electron microprobe measurements of amphiboles (Table 2: log K/Ca = −1.72/−2.25 as average results for Z102 and Z103G). The abundance of amphibole in the clinopyroxenites can be calculated by assuming that ^{37}Ar released between 1000 and 1140°C represents the total Ca bond in amphibole. This results in 0.26% and 0.24% Ca associated with amphibole in Z102 and Z103G total separates, respectively. As Z102/Z103G amphiboles have ~12% CaO or 8.6% Ca (Table 2), amphibole concentrations of 3.0% and 2.8% are calculated for Z102 and Z103G separates, respectively.

The amphibole and pyroxene reservoirs are also associated with Cl-derived ^{38}Ar peaks (Fig. 6). In the case of the amphiboles, the Ar derived Cl/K (or Cl/Ca) ratios are compatible with EMPA Cl/K ratios, indicating that Cl measured via ^{38}Ar represents Cl of the amphibole lattice and not Cl of some additional minor phases. For Z102 pyroxene, the Ar derived Cl/Ca ratio (8.5×10^{-3}) is about four times higher than the EMPA average of orthopyroxene and clinopyroxene [$(2.4 \pm 1.0) \times 10^{-3}$, calculated for 50% modal abundances]. In spite of the EMPA uncertainties, a factor of 4 is a clear hint that most of the Cl is not released from the pyroxene lattice, but from completely encapsuled Cl-rich inclusions upon melting. In turn these inclusions have Ar derived Cl/K ratios of ~6.0 (or twice as much, if only 50% K is hosted by the inclusions) and, therefore, cannot be amphiboles, of which the Cl/K ratio is about 2.4 (obtained by EMPA on Z102 amphiboles). The most probable Cl hosts are microfluid inclusions which did not decrepitate before melting. Fluid inclusions containing NaCl and KCl are abun-

dant within clinopyroxenite vein rock Z102 and are described in Kurat et al. (1993); most of them are rather small ranging from 2 to 15 μm in size. According to the above calculations, 50% of the high temperature K-reservoir is hosted by the inclusions. On the other hand, in the case of Z103G pyroxene Cl/Ca ratios obtained by argon isotopes and EMPA are compatible, so that it is not necessary to advoke fluid inclusions as host of the Cl.

Besides pyroxene and amphibole reservoirs, the degassing patterns of ^{36}Ar, Cl-derived ^{38}Ar, and excess ^{40}Ar (Fig. 6) show well defined low temperature reservoirs for Z102. Serpentine is one of the minor phases in Z102, and it contains significant amounts of Cl. About 4% serpentine would be sufficient to account for the observed Cl-derived ^{38}Ar (corresponding to 235 ppm Cl in the low temperature peak from 620–860°C), which is possible to be reconciled with observed modal abundances. Moreover, the (Ar derived) Cl/K ratio of 12 in the low temperature reservoir is compatible with the EMPA Cl/K ratio of 18 ± 11 obtained for serpentine. Although we cannot exclude the decrepitation of larger fluid inclusions at these temperatures, we believe that a significant part of the low temperature release is due to serpentine, for which a similarly low degassing temperature can be inferred by data of Lopez-Martinez et al. (1992).

Once we have identified the carrier phases of Ar released at different temperature ranges, we are able to discuss the argon isotopic composition with respect to the carrier phases and their genesis. Figure 7 shows ^{40}Ar/^{36}Ar ratios vs. 1/^{36}Ar, a plot commonly used to test for local contamination by atmospheric Ar. We assigned different symbols to the low, medium (amphibole), and high (pyroxene) temperature reservoirs. In the case of Z102 (Fig. 7a), atmospheric contamination is evident for the low temperature fractions. The data plot along a straight line: the higher the ^{36}Ar concentration, the closer the ^{40}Ar/^{36}Ar ratio comes to the atmospheric value. This is not the case for the amphibole and pyroxene reservoirs that follow a trend parallel to the x-axis. Average ^{40}Ar/^{36}Ar ratios are 1500 ± 400 for Z102 amphibole and 1300 ± 200 for Z102 (microinclusions in) pyroxene. For Z103G (Fig. 7b), a contamination correlation seems to be present for the low temperature fractions as well, but not very well defined. The medium temperature fractions representing the amphibole reservoir seem to be uncontaminated, defining an average value of ^{40}Ar/^{36}Ar = 6500 ± 700. Two values of the pyroxene reservoir are indistinguishable from this value, however, at higher temperatures ^{40}Ar/^{36}Ar ratios decrease to almost atmospheric values. Insufficient blank correction is a possible source of error due to the very low amounts of ^{36}Ar in these temperature fractions; another explanation could be a separate phase besides pyroxene, e.g., again microinclusions or other poikilitically included mineral phases. Though we cannot come to a definite conclusion regarding the Z103G high temperature carrier phase, a high ^{40}Ar/^{36}Ar component seems also to be present in the clinopyroxene.

4.4. Chronology of Peridotite Differentiation and Mantle Metasomatism

We earlier questioned, if ^{40}Ar is due to in situ K decay during mantle residence times (this would require >1Ga

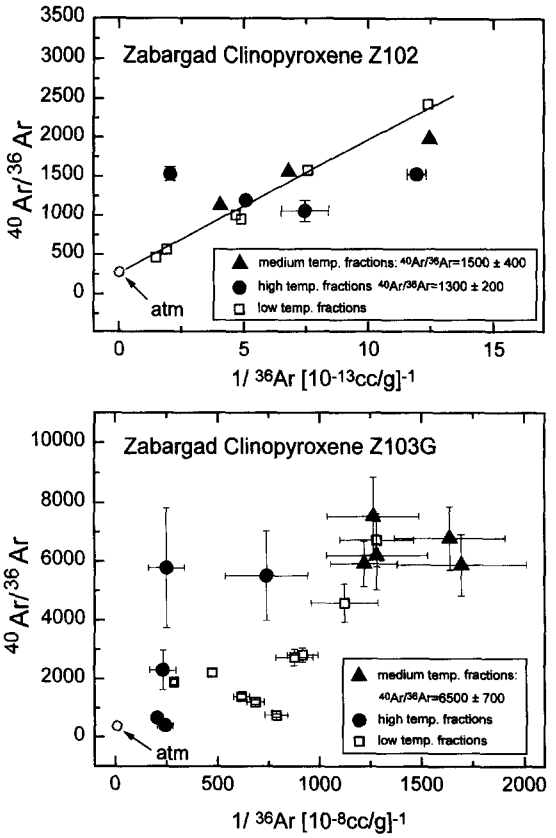

Fig. 7. ^{40}Ar/^{36}Ar ratios vs. 1/^{36}Ar plots of clinopyroxene separates. Trapped ^{40}Ar/^{36}Ar ratios range up to 8000. Low, medium (amphibole), and high temperature (pyroxene) reservoirs have different isotopic compositions, reflecting different sources.

^{40}Ar accumulation) or if it was trapped rather recently. In the latter case ^{40}Ar/^{36}Ar ratios represent a characteristic signature of the source Ar was trapped from. Figure 8a and 8b show isochrone plots with ^{36}Ar/^{40}Ar vs. ^{39}Ar/^{40}Ar ratios of Z102 and Z103G. If samples contain a mixture of in situ radiogenic and trapped Ar, they plot on a straight line, where the y- and x-intercepts correspond to the isotopic composition of trapped Ar and the age of the sample, respectively. For the Z103G amphibole reservoir (five points) a fit gives a horizontal straight line (Fig. 8b) corresponding to a zero age and indicating that Ar with ^{40}Ar/^{36}Ar = 6500 ± 700 was trapped rather recently. The lower confidence band points to a ^{39}Ar/^{40}Ar intercept > 0.082, corresponding to an upper age limit of 250 Ma. Similar zero age trends parallel to the x-axis are also defined by Z102 medium and high temperature reservoirs (Fig. 8a) indicating recent formation of amphibole and recent trapping of microinclusions into the pyroxene, as well as associated trapped Ar. Note that the nonsystematic scatter of the low temperature fractions in Z102 is due to atmospheric contamination, as inferred above. The same holds for the low temperature fractions of Z103G (Fig. 8b).

An alternate approach to resolve the contradiction of varying ^{40}Ar/^{36}Ar ratios within Z103G high temperature fractions (Figs. 7, 8) would be to regard the array in Fig. 8b as an isochron. This would imply a trapped Ar component of nearly atmospheric composition and a radiogenic component

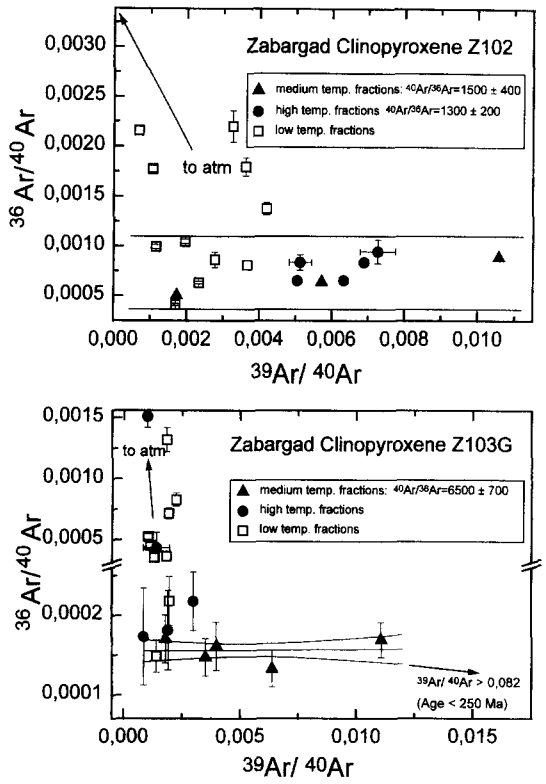

Fig. 8. Isochrone plot with $^{36}Ar/^{40}Ar$ vs. $^{39}Ar/^{40}Ar$ ratios for Z102 and Z103G clinopyroxene separates. Rocks containing a mixture of in situ radiogenic and trapped Ar should plot on a straight line, where the y- and x-intercepts correspond to the isotopic composition of trapped Ar and the age of the sample, respectively. Horizontal zero age trends are defined by medium and Z102 high temperature fractions assigned to amphiboles and micro fluid inclusions of Z102. This suggests recent formation of amphibole and recent trapping of microinclusions into the pyroxene as well as associated trapped Ar.

corresponding to an age of ~3.5 Ga. However, this seems to be unrealistically high for the lithospheric mantle beneath the Arabian-Nubian plate, as indicated by other chronometers. Sm-Nd data of Zabargad peridotites measured by Brueckner at al. (1988, 1995) plot along a line in the Sm-Nd isochron plot, which is included by an array of Sm-Nd data of Arabian xenoliths (Henjes-Kunst et al., 1990). The array is interpreted as the time of differentiation of lithospheric mantle and crust during the Pan-African 650–850 Ma ago. Henjes-Kunst et al. (1990) also found evidence for recent mantle metasomatism manifested in some xenoliths. In their type IB xenoliths a first period of metasomatism induced hydrous minerals, e.g., Cr-pargasite and minor Ba-phlogopite, while a second metasomatism caused growth of intergranular amphibole in a further texturally different xenolith group (their subtype IA2), as well as secondary amphibole growth and formation of melt patches in type IB xenoliths. Type IB minerals form a horizontal (zero age) array in the Sm-Nd isochron plot, indicating that the two events represent recent, but obviously distinct periods of metasomatism. Both were suggested to be linked to upper mantle fractionation processes during evolution of the Red Sea rift.

We conclude, that Z102 and Z103G amphiboles as well as Z102 microinclusions in pyroxene, that also show horizontal zero age arrays in Fig. 8, most probably formed (or were trapped) during such recent mantle metasomatism, which probably affected the mantle region around the Zabargad. Amphibole formation took place during interaction with different mantle-derived fluids, as we will show in more detail in the next sections. These mantle fluids obviously carried Ar with distinctly different isotopic composition, much higher than the atmosphere-like composition of Ar trapped in Z28 hornblende.

It should also be mentioned that, based on neodymium, strontium, lead, and osmium isotope data, Brueckner et al. (1995) made the much more far-reaching suggestion that Zabargad peridotites were already intruded into the lower crust during the Pan-African. This seems difficult to reconcile with the recent ages of the Z102 and Z103G amphiboles, which formed in interaction with mantle fluids.

4.5. Different Generations of Amphibole in Zabargad Peridotites

Evidence for various metasomatism events are ubiquitous in Zabargad peridotites. Kurat et al. (1993) already showed evidence that Zabargad vein rocks were subjected to varying fluid-rock interactions and noted different amphibole generations. Based on textural relationships, Agrinier et al. (1993) classified three types of amphibole which were related to different stages during the uplift and final emplacement of the peridotite diapir. They describe a first generation of scarce Ti-pargasites (characteristic brown amphibole occurring as interstitial crystals, e.g., as observed also in our sample Z34) which was related to early crystallization from small amounts of mantle-derived H_2O-bearing fluids at 900–1000°C before uplift-related deformation. A second generation consisting of Cr-pargasites (abundant pale green amphibole replacing clinopyroxene) formed by reaction between the peridotites and a sodium/potassium-bearing fluid at temperatures of around 700–800°C and grew synchronously with the diapiric uplift. The third generation, localized in shear zones and veins, was estimated to have crystallized at temperatures of 450–700°C, again from a sodium/potassium-bearing fluid, but originating outside the peridotites, most probably seawater that invaded the diapir during the final emplacement. The classification is supported by hydrogen and strontium isotope ratios, which is shown in Fig. 9, reproduced from Agrinier et al. (1993). The mantle types I and II have lower $^{87}Sr/^{86}Sr$ ratios of ≤ 0.7045 than late type III (≥ 0.7055), and lower δD values, which plot in a field typical for mantle material. Stars are whole rock data by Kawahata et al. (1987) of hydrothermally altered submarine basalt. Type III amphiboles have strontium and hydrogen isotope ratios compatible with formation by interaction with seawater.

Amphibole in our samples also fit into that classification scheme: the occurrence as dikelet, relatively low Ti, Cr, and K content are sufficient to classify Z28 as type III amphibole. One should also note, that in the Southern massif (where Z28 was collected) most amphiboles (four out of five) are type III amphiboles (Agrinier et al., 1993). So for Z28 this

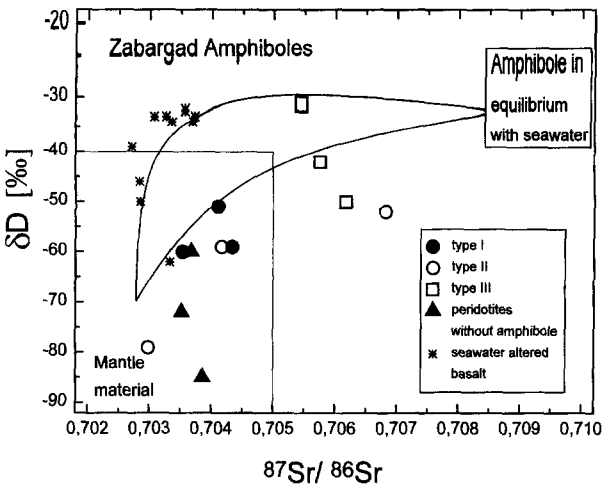

Fig. 9. Amphiboles of type I and II plot in a field typical for mantle material, in contrast to type III amphiboles (reproduced from Agrinier et al., 1993). Sketched curves exemplify seawater hydrothermal amphibole growth with different Sr contents and low water contents (0.2%). Seawater hydrothermally altered basalt whole rock data (stars) by Kawahata et al. (1987).

implies formation by interaction with fluids derived from seawater, which also explains the $(^{40}Ar/^{36}Ar)_{exc}$ ratio of 305 that is only slightly above the atmospheric ratio. Morphological criteria of amphiboles occurring within clinopyroxenites Z102 (and Z103G) suggest type I or II. Furthermore, there are no descriptions of type III amphiboles on the central peridotite hill, where the clinopyroxenites were collected. When plotted in a K vs. Ti diagram (Fig. 10a), the data indicate type II, except for one Z102 analysis, which corresponds to type I amphibole. Amphibole data from Brandstätter et al. (1993) are also included. Ten out of nineteen analyses plot within the type II regime in the K vs. Ti diagram, allowing a preliminary chemical classification. In many cases samples containing type I amphibole also contain type II amphibole (Z17G, Z15, Z102, Z118H). Type I and II amphiboles should also be different when plotted in a Al^{IV} vs. $(Na + K)_A$ diagram (see Agrinier et al., 1993). However, the calculation of Al^{IV} substituting Si and especially of (Na+K) in the M_4 and the A site are quite sensitive to uncertainties of the H_2O^+ content, which was not measured in our samples. Nevertheless, when taking an H_2O^+ content of 2% measured by Agrinier et al. (1993), the two types plot in two distinct fields, indicated by the open loop (type I) and the straight line (type II) in Fig. 10b.

As type I/II amphiboles of the clinopyroxenites originated by interaction with mantle-derived H_2O-bearing fluids, it is not surprising that $(^{40}Ar/^{36}Ar)_{exc}$ ratios of the trapped Ar are as high as 1500 ± 400 and 6500 ± 700 for Z102 and Z103G amphibole, respectively, in contrast to the atmosphere like low ratio of Z28 hornblende.

4.6. $^{40}Ar/^{36}Ar$ Ratios of Mantle Derived Argon

$^{40}Ar/^{36}Ar$ ratios higher than the atmospheric value have long been known to exist in even zero age mantle-derived rocks and their implications for the degassing of part of the Earth's mantle had also been discussed quite early (Ozima, 1975). The essential feature is that a depleted (upper) mantle with high ratios is suggestive of an early massive outgassing of this reservoir, allowing the radiogenic component (^{40}Ar) to accumulate relative to the rather small remaining primordial component (^{36}Ar). The same mechanism seems to be responsibe for MORB ^{129}Xe excesses, i.e., post-degassing accumulation of the decay product of short-lived ^{129}I.

Stepheating and crushing of MORB glasses of the Atlantic, Pacific, and Indian oceans (Sarda et al., 1985; Staudacher et al., 1989) yielded the highest $(^{40}Ar/^{36}Ar)_{exc}$ ratios so far from upper mantle-derived rocks (up to 30 000). Lower ratios obviously had to be attributed to an atmospheric component. While Marty and Ozima (1986) and Jambon et al. (1985) presented some evidence that the atmospheric contaminant is most probably dissolved in the glass and that the gases of mantle origin are present in the vesicle population, Fisher (1994) showed that the vesicle Ar is neither more radiogenic than the glass dissolved Ar nor can it be regarded as the pure upper mantle endmember in most cases.

A mantle substructure as far as argon isotopes are concerned was early indicated by the work of Kaneoka and Takaoka (1978) and proposed by Kaneoka et al. (1978).

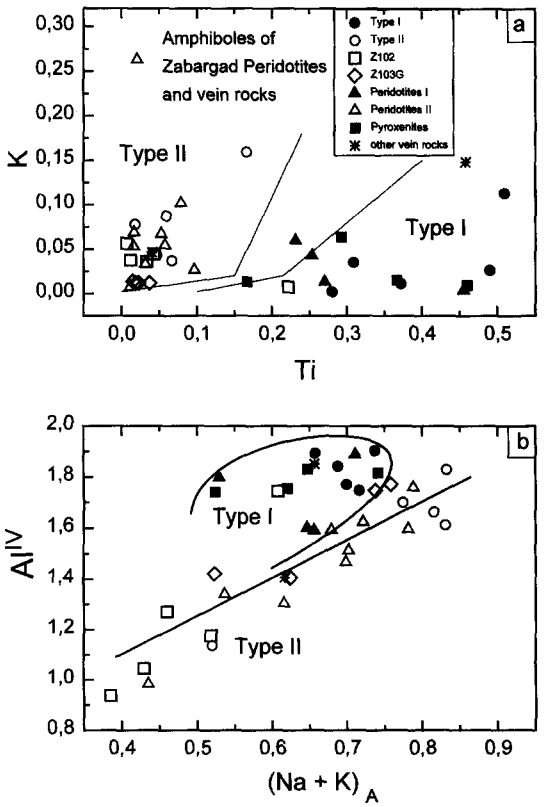

Fig. 10. Diagrams showing (a) K vs. Ti and (b) Al^{IV} vs. $(Na + K)_A$ of Zabargad amphiboles. Type I and II amphiboles can be classified according to the different areas in the K vs. Ti diagram; in the Al^{IV} vs. $(Na + K)_A$ plot as well distinct fields are occupied by type I (open loop) and type II amphiboles (array along straight line). Z102 and Z103G data from this work; also included are type I and II amphiboles classified by Agrinier et al. (1993) and amphibole data from other Zabargad peridotites and associated vein rocks measured by Brandstätter et al. (1993).

They concluded that high $^{40}Ar/^{36}Ar$ ratios of more than 1000 are present beneath the continental crust (S.A. Kimberlite field) down to 120 km, beneath hot spot areas (Hawaii) down to 50 km, but lower than 1000 below such depths. Surprisingly low $^{40}Ar/^{36}Ar$ values were confirmed subsequently for the Hawaii hot spot area (Kyser and Rison, 1982; Kaneoka et al., 1983). These results were interpreted in terms of mixing of a high ratio-MORB component and an atmosphere-like low ratio component with variable degree, with the low ratio component representing either atmospheric contamination, or an undepleted mantle reservoir. $^{40}Ar/^{36}Ar$ ratios as low as 390 obtained on Loihi sea mount samples, coupled with an undoubtedly nonatmospheric, primordial He signature even higher than MORB ($^{3}He/^{4}He = 5 \times 10^{-5}$ compared to $1-2 \times 10^{-5}$), led Allègre et al. (1986) and Staudacher et al. (1986) to the conclusion that the low $^{40}Ar/^{36}Ar$ ratio would be representative of the undegassed lower mantle. The lack of ^{129}Xe excesses also seemed to confirm the undegassed nature of this reservoir that retained all Xe isotopes (not only the ^{129}I decay product ^{129}Xe).

However, a scenario which ascribes an atmosphere-like noble gas component of oceanic island basalts to the lower mantle was challenged by several authors (e.g., Fisher, 1985; Patterson et al., 1990). Subsequent investigations by Hiyagon et al. (1992) and Honda et al. (1993) revealed the presence of solar-like neon in the mantle, which implied that most of oceanic island basalt glasses contain significant amounts of atmospheric neon. This seems to be the case for Ar, too, which is obviously admixed during magma ascent, possibly by seawater circulating deep within the oceanic crust (Farley and Craig, 1994). Helium is not affected because of its low concentration in both the atmosphere and seawater. Studies on Samoan xenoliths seem to point to a lower mantle $^{40}Ar/^{36}Ar$ ratio of more than 5000 (Poreda and Farley, 1992). In this case, $^{40}Ar/^{36}Ar$ ratios lower than 5000 within Ar retentive mantle xenoliths and peridotites of deep origin imply the presence of atmospheric Ar within great depths of the mantle. The essential perception in the course of the above quoted work was that many mantle derived rocks are contaminated by atmosphere-type noble gases and that contamination in many cases occurs in a nontrivial, subtle way that means not just by an insufficient system blank correction or the release of adsorbed surficial gases.

Relatively low $(^{40}Ar/^{36}Ar)_{exc}$ ratios (when compared to values assigned to the upper or lower mantle today) have also been observed for ultramafic xenoliths, and in the few cases where mineral separates were analyzed, inhomogeneities were not uncommon. Different trapped $^{40}Ar/^{36}Ar$ ratios of different minerals of ultramafic xenoliths observed by Kyser and Rison (1982) were interpreted to be caused by specific degrees of isotopic exchange with the surrounding magma, thus retaining variable ratios during different stages of their uplift history. This kind of limited isotopic exchange has also been observed by Kaneoka et al. (1983). Different $^{40}Ar/^{36}Ar$ ratios are observed within Zabargad clinopyroxenite vein rocks as well, and we also regard them as indigenous to the source they were trapped from. Z102 and Z103G amphiboles are obviously derived from mantle fluids at considerable depths. They contain distinctly different $^{40}Ar_{exc}/^{36}Ar$ ratios. In the case of Z102, low $^{40}Ar_{exc}/^{36}Ar$ ratios of 1500 ± 400 for amphibole and 1300 ± 200 for microinclusions in pyroxene require the presence of an atmospheric component within the mantle regions, where amphiboles and inclusions trapped their Ar. In the case of Z103G amphibole ($^{40}Ar_{exc}/^{36}Ar = 6500 \pm 700$), an atmospheric component is not compelling. Another possibility is binary mixing of an upper mantle and a plume component, as there is evidence for measurable plume noble gas contributions (most probably of the Afar plume) all along the Red Sea ridge (Moreira et al., 1996).

4.7. Characterization of Metasomatizing Mantle Fluids via Argon Isotopes

Beyond geochronological applications, the ^{40}Ar-^{39}Ar -stepheating technique is not only capable of identifying carrier phases of isotopically diverse Ar (see above). The technique is also able to detect K and Cl correlated argon isotopes at K and Cl concentrations in the order of several ppm. It is, therefore, possible to sensitively measure K, Cl, and Ar in phases formed by fluid-rock interaction and to a certain extent characterize the fluids which took part in the formation of these phases. Table 3 shows the $^{40}Ar_{exc}/^{36}Ar$, $^{40}Ar_{exc}/Cl$, K/Cl, and $^{40}Ar_{exc}/K$ ratio as well as $^{40}Ar_{exc}$, ^{36}Ar, K, and Cl contents of Z102, Z103G, and Z28 amphibole and pyroxene reservoirs. In the middle part of the table, Ar, K, and Cl concentrations are given referring to the mass of the whole separate. For the amphiboles, concentrations are furthermore given according to the above calculated abundances of amphiboles of ~3 and 2.8% within the two clinopyroxene separates (lower part of Table 3).

Within Z102 pyroxene-fluid inclusions Cl and K reside most probably in NaCl and KCl. Fluid inclusions in pyroxene range from 2 to 15 μm in size (Kurat et al., 1993). Both primary isolated inclusions and secondary inclusions occurring in trails were obviously formed before deformation, i.e., in the mantle. The fluid inclusions contain less than 50% minerals (NaCl and carbonates) and biphased (liquid/gaseous) CO_2. Homogenization of CO_2 in the various fluid inclusions occurs in the liquid by disappearance of the gas bubble at temperatures clustering at 30°C. This can be calculated to correspond to densities of 0.7 g/cm^3 and trapping pressures of about 3 kb for a reference temperature of 1000°C. These values are, however, minima as due to deformation of the pyroxene densities most probably have significantly decreased. From the Cl concentration of 434 ppm a NaCl abundance of 0.07 wt% can be inferred. Assuming that wt% corresponds approximately to vol% and that 25% of the inclusion volume is NaCl, one furthermore can calculate 0.28 vol% inclusions, which is a quite reasonable value for the rock.

As outlined above, Z103G and Z102 amphibole and Z102 pyroxene microinclusions are phases which formed by fluid-rock interaction during rather recent mantle metasomatism. Calculated average ratios of $^{40}Ar_{exc}/Cl$, $^{40}Ar_{exc}/K$, and K/Cl of these three phases obviously differ from values for Z103G pyroxene (Table 3). This may reflect the circumstance, that the genesis of Z103G pyroxene is not linked to recent mantle metasomatism. In contrast, the two amphiboles and Z102 microinclusions have ratios much more similar to each other, in particular regarding $^{40}Ar_{exc}/Cl$ ratios. This could be taken

Table 3. Ar, K, and Cl abundances and elemental ratios characterizing the Ar carrier phases from clinopyroxenites Z102 and Z103G and their parental fluids.

Sample	Z102	Z102	Z103G	Z103G	Z28 #1/#2	Zaire coated diamonds[a]
Temperature fractions	13–14	16–18	13–15[b]	17–19	all	—
Host phase	amphibole	micro fluid inclusions in pyroxene	amphibole	pyroxene	amphibole	microinclusions
$^{40}Ar_{exc}/^{36}Ar$	1500 ± 400	1300 ± 200	6500 ± 700	2000–6000	305 ± 3/315	600–15000
$^{40}Ar_{exc}/Cl$[c]	.28	.26	.27	.45	.030/.031	52
K/Cl	.28	.18	.23	.064	.229/.239	2–3
$^{40}Ar_{exc}/K$[c]	1.0	1.5	1.2	6.9	.073/.105	21
Measured concentrations, referred to clinopyroxene and hornblende total separates:						
$^{40}Ar_{exc}$ [10^{-8} ccSTP/g]	51	112	15.6	40	116/128	80–300/300–700
^{36}Ar [10^{-8} ccSTP/g]	.039	.082	.0024	.097	.380/.407	0.03–0.23
K [ppm]	51	76	13.3	5.8	1597/1222	0.6–65
Cl [ppm]	183	434	58	90	3828/4161	0.2–17.3
Calculated concentrations in host phases[d]:						
abundance of host phase	3.0 wt.%	0.28 vol.%[f]	2.8 wt.%	95 wt.%		
$^{40}Ar_{exc}$ [10^{-8} ccSTP/g]	1690	—	557	42.2		
^{36}Ar [10^{-8} ccSTP/g]	1.30		0.086	.102		
K [ppm][e]	1700	—	475	6.1		
	1715 ± 173		519 ± 42	<84		
Cl [ppm][e]	6100	—	2071	95		
	4100 ± 752		1875 ± 171	<200		

[a] Turner et al. (1990); $^{40}Ar_{exc}$ for cores and coats, respectively.
[b] Amphibole Ca without fraction 15, which is probably already influenced by pyroxene release.
[c] Ratios are given in [10^{-8} ccSTP/g ppm].
[d] Abundances of the host phases are calculated as described in the text.
[e] Average EMPA results added for comparison (in spite of large uncertainties for pyroxene)—data are in good agreement.
[f] Inclusion content is calculated assuming Cl resides in NaCl constituting 25 vol% of the inclusions, as described in Kurat et al. (1993) and in the text.

as hint that these phases were derived from a common parent fluid. It is, however, difficult to reconcile the observed elemental abundances with a simple scheme of fluid source mixing, in particular regarding the fact that the amphiboles formed from a H_2O-bearing fluid, while the fluid inclusions in pyroxene are devoid of H_2O and consist mainly of CO_2. At least three stages of fluid modification with three different participating fluids would be required in order to account for the observed features: one possible scenario is that a common parent fluid with $^{40}Ar/^{36}Ar$ = 6500, $^{40}Ar_{exc}/Cl$ = 0.27, and $^{40}Ar_{exc}/K$ = 0.7 splits into two different fluids; the first is later enriched in appropriate amounts of H_2O and K to form Z103G amphibole, which formed after deformation. The second fluid could have been incorporated into primary inclusions of Z31, and after addition of some atmospheric argon into secondary Z31 and microinclusions of Z102 pyroxene, which are devoid of water and formed before main deformation. Addition of atmospheric argon shifts the $^{40}Ar/^{36}Ar$ ratios down significantly, but does not change very much the absolute concentration of ^{40}Ar or, therefore, the ratios computed with ^{40}Ar, K, and Cl (see the following section). Some further H_2O and K is needed to form Z102 amphibole later on after deformation. Such H_2O and K-bearing fluids are in accord with the formation scenario of type II amphibole described by Agrinier et al. (1993). Of course this scenario is not unique, and processes involving fluid dehydration could have been involved as well.

Independent of such a scenario are some considerations from a more general point of view: $^{40}Ar_{exc}/Cl$ ratios of all Zabargad samples, are 2 orders of magnitude lower than those of Zaire cubic diamonds (Turner et al., 1990) also given in Table 3. These ratios, clustering at 52 [10^{-8} ccSTP/g ppm], were found to be similar to a mantle olivine from Tanzania. The authors concluded that this value might be representative of a quite homogeneous upper mantle source. This conclusion was derived from one mantle olivine only and may probably be rather characteristic for Zaire cubic diamonds than for peridotites and associated rocks, as our samples exhibit much lower ratios. However, the difference could also be explained by the exceptional enrichment (a factor 10–100) of the halogens in Zabargad rocks when compared to ultramafic xenoliths found in the course of previous studies (Kurat et al., 1993; Jagoutz et al., 1979). But data are still scarce and future investigations may show whether the mantle source (or at least certain regions) have homogenous $^{40}Ar_{exc}/Cl$-ratios or not.

4.8. Light Noble Gases

Light noble gases (^4He, ^{20}Ne, ^{36}Ar, and ^{40}Ar) were measured in four unirradiated samples, two vein rocks, (clinopyroxenite Z103G and orthopyoxenite Z31), and two peridotites (harzburgite Z103H and lherzolite Z34). The results are given in Table 4.

The absolute concentrations of ^{4}He, ^{20}Ne, and ^{36}Ar are within the broad range of terrestrial rocks and come closest to submarine volcanic rocks (Ozima and Podosek, 1983). Noble gas concentrations scatter somewhat, and there seems to be a trend of higher noble gas concentrations in pyroxenite vein rocks than in peridotite hosts, which may be due to the better solubility of noble gases in pyroxene as compared to olivine. Noble gas concentrations in spinel lherzolites from a quaternary basalt flow and underlying tuffs at San Carlos, Arizona (Bernatowicz, 1981) are lower by a factor of ten in ^{20}Ne, and even more severely in ^{36}Ar, resulting in a $^{20}Ne/^{36}Ar$ ratio about ten times higher than Zabargad rocks. Spinel lherzolite xenoliths from Hawaii (Kyser and Rison, 1982) and Samoan Xenoliths (Poreda and Farley, 1992) have similar ^{20}Ne, but slightly lower ^{36}Ar concentrations than our samples. The $^{40}Ar/^{36}Ar$ ratios found for nonirradiated Zabargad samples are well within the range determined by ^{40}Ar-^{39}Ar analysis of the irradiated samples, except for the low $^{40}Ar/^{36}Ar$ ratio of harzburgite Z103H. Z103G was the only sample analyzed both in Mainz and Heidelberg. ^{36}Ar and ^{40}Ar contents differ by about a factor of two, which demonstrates the inhomogeneous distribution of noble gases and/or their carrier phases in the sample.

Special attention must be given to the data of the orthopyroxenite vein rock Z31. Z31#1 was analyzed by total fusion, Z31#2 was crushed in five steps, while two crushed aliquots (TF#a and TF#b) were fused subsequently. As two aliquots were measured, however, it was not possible to avoid exposure to air after crushing. TF#a and TF#b are quite similar except for the ^{36}Ar concentration, coupled with a rather low $^{40}Ar/^{36}Ar$ ratio of TF#a. As sample Z31 TF#a was exposed to lab air much longer and had significantly higher values of ^{84}Kr and ^{132}Xe, we conclude that some atmospheric contamination occurred most probably during storing after crushing. If the difference in ^{36}Ar is ascribed to air, then ^{40}Ar of TF#a can be corrected to 440 instead of 481 $\times 10^{-8}$ ccSTP/g, in much better agreement to 432 $\times 10^{-8}$ ccSTP/g of TF#b. For these reasons TF#a is excluded from the discussion below. The added gas amounts of sample #2 are in good agreement with sample #1.

Isotopic abundances and ratios throughout the five crushing steps and the final total fusion step are shown in Fig. 11a and b, respectively. Isotopic ratios are correlated: in the advanced crushing steps both radiogenic isotopes (^{4}He, ^{40}Ar) are progressively enriched by a factor of two with respect to the nonradiogenic isotopes, while the $^{4}He/^{40}Ar$ ratio increases only by 13%, but still fitting a well defined correlation (Fig. 11b). The relative constancy of the $^{4}He/^{40}Ar$ ratio (ranging between 0.135 and 0.156), compared to the much larger spread of other isotopic and elemental ratios, excludes fractionation as reason for the correlations. The clear correlation of isotopic ratios with increasing crushing steps can only be explained by the presence of two different types or generations of inclusions which differ with respect to structural stability against mechanical crushing. Fluid inclusions in orthopyroxenite Z31 show similar characteristics as in clinopyroxenite Z102 (see above). Primary isolated inclusions tend to be larger than the much more numerous secondary inclusions occurring in trails. Considering size alone, larger inclusions would be probably less resistant against crushing, if both inclusion types are located in an intact crystal lattice. However, the latter seems to be the case for primary inclusions only. Secondary inclusions are present along annealed fractures, which are most probably crushed more easily. Therefore, it is justified to assume that the noble gas component released in the advanced crushing steps is hosted mainly by primary inclusions, while the first crushing steps release gases mostly from secondary inclusions. Inclusion populations have been studied in this vein rock in a previous study, and Fig. 13 shows two inclusion trails (reproduced from Kurat et al., 1993).

What about the origin of the two different noble gas com-

Table 4. Noble gas concentrations (in 10^{-8} ccSTP/g), and isotopic ratios obtained by total fusion (TF) of nonirradiated samples, two vein rocks, and two peridotites. For Z31 data were also obtained by stepcrushing and subsequent total fusion (Z31#2). Uncertainties of absolute noble gas concentrations are 5%.

Samples	^{4}He	^{20}Ne	^{36}Ar	^{40}Ar	$^{40}Ar/^{36}Ar$	$^{4}He/^{40}Ar$	$^{20}Ne/^{36}Ar$
Z34	49.2	.029	.134	280	2090	0.176	0.216
Z103G	100	.040	.105	334	3181	0.299	0.381
Z103G[a]			.040	109.6	2740		
Z103H	12.2	.018	.125	85.9	687	0.142	0.144
Z31#1	115	.053	.177	945	5339	0.122	0.299
Z31#2[b]	107.2	.0637	.265	687.9	2596	0.156	0.240
Z31#2:							
Z31 20[c]	6.30	.0077	.0407	46.8	1150	0.135	0.189
Z31 40[c]	13.3	.0102	.0488	90.2	1848	0.147	0.209
Z31 50[c]	9.49	.0063	.0277	62.3	2249	0.152	0.227
Z31 50[c]	5.49	.0029	.0115	35.2	3061	0.156	0.252
Z31 50[c]	3.32	.0016	.00625	21.4	3424	0.155	0.256
Z31 crush	37.9	.0287	.1390	255.9	1841	0.148	0.206
Z31 TF#a	69.0	.036	.266	481	1808	0.143	0.135
Z31 TF#b	69.3	.035	.126	432	3429	0.160	0.278

[a] ^{40}Ar-^{39}Ar analysis from Table 1.
[b] Added amount of five crushing steps and subsequent total fusion.
[c] Denotes the number of crushings.

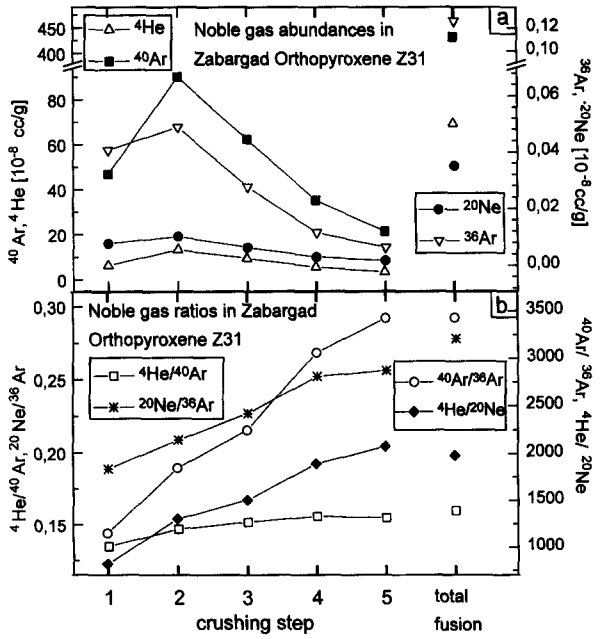

Fig. 11. Elemental abundances and noble gas ratios for five crushing steps and subsequent total fusion of Z31 orthopyoxene. Isotope ratios show a clear correlation with crushing step, indicating separation of different inclusion types, most probably primary and secondary, as described in the text.

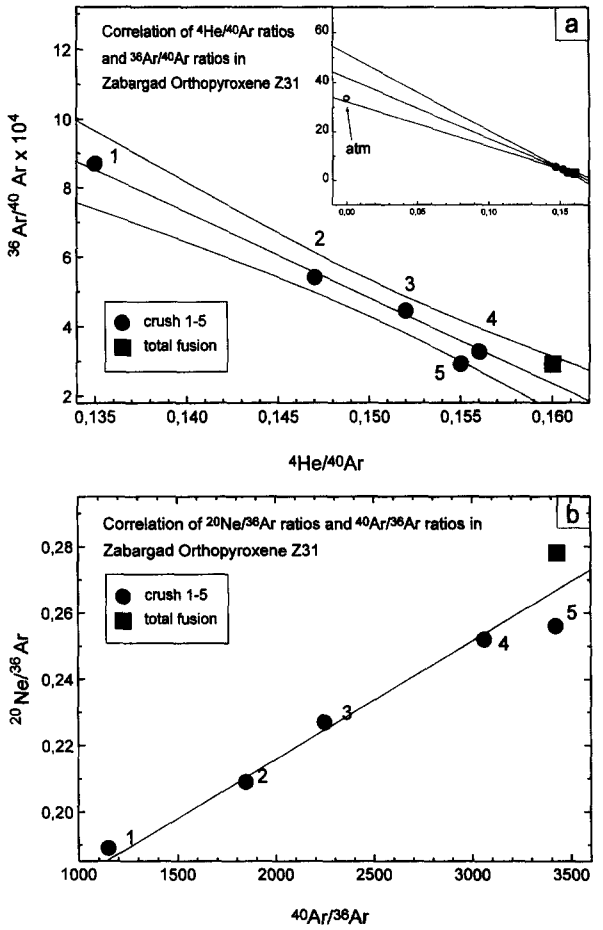

Fig. 12. Correlation of (a) $^{36}Ar/^{40}Ar$ with $^{4}He/^{40}Ar$ ratios and (b) $^{20}Ne/^{36}Ar$ with $^{40}Ar/^{36}Ar$ ratios for Z31. Correlations evidence mixing of mantle and atmosphere type noble gases within the peridotite source region.

ponents? Figure 12a shows explicitly the correlation between $^{4}He/^{40}Ar$ and $^{36}Ar/^{40}Ar$ ratios. The line fit extrapolated to low $^{4}He/^{40}Ar$ ratios results in an $^{40}Ar/^{36}Ar$ intercept indistinguishable from atmospheric argon at the 95% confidence level. This feature can be explained by the radiogenic isotopes indigenous to their mantle source that later was contaminated by a source containing atmosphere type noble gases, rich in ^{36}Ar and low in ^{4}He. Both inclusion types that are separated by stepcrushing, contain the mantle component, but are contaminated to a different degree with the atmospheric component, which constitutes nearly all ^{36}Ar, but only a small fraction of the total ^{40}Ar. Figure 12b shows the correlation of $^{20}Ne/^{36}Ar$ and $^{40}Ar/^{36}Ar$ ratios. If the line fit is extrapolated towards the $^{40}Ar/^{36}Ar$ ratio of 30000 as is assumed for the pure upper mantle source, this would correspond to an $^{20}Ne/^{36}Ar$ ratio of about 0.9–1.2, in agreement with values assigned to the unfractionated upper mantle (Staudacher et al., 1989). When extrapolating the line fit to the atmospheric $^{40}Ar/^{36}Ar$ ratio of 295.5, the $^{20}Ne/^{36}Ar$ ratio would become ~0.15, which is similar to atmosphere type noble gases dissolved in water. So the two components hosted by the primary and secondary inclusions may be interpreted as mixture of MORB and atmosphere type noble gases. In this respect the correlation in Fig. 12b suggests the presence of mantle ^{20}Ne, a suggestion that can, however, only be clarified by additional neon isotopic data. On the other hand, as both inclusion types were trapped before deformation and uplift of the peridotite complex (Kurat et al., 1993), admixing of atmosphere like Ar must have occurred in the peridotite source region. This again requires the presence of atmospheric Ar in this mantle region, as was already

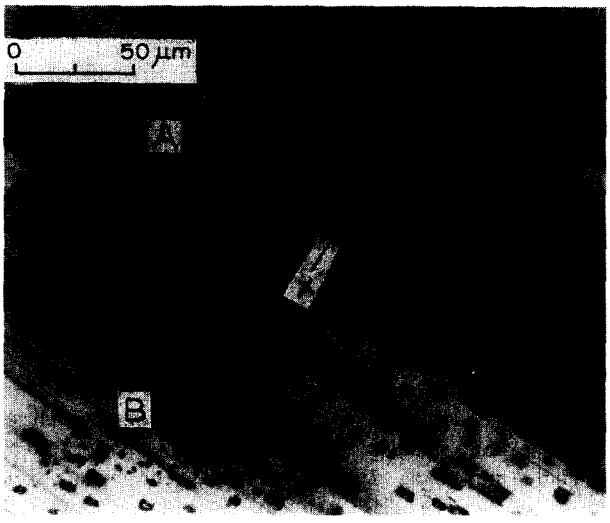

Fig. 13. Different inclusion trails in orthopyoxenite Z31 (reproduced from Kurat et al., 1993). *X*: inclusion with two-phase (liquid-vapor) CO_2 at room temperature.

concluded from our results on Z102 and Z103G clinopyroxenites.

Our results imply that two different noble gas components survived close to each other in the same piece of rock at the cm scale. This signifies that after trapping which occurred obviously before deformation and fast uplift, equilibration did not take place under mantle conditions, apparently not even for He. This is a surprising result, even if we consider the probable case, that the mantle metasomatism introducing the fluid inclusions happened rather recently, and, therefore, the residence time within the mantle was no more than a few Ma. It also indicates that the very similar isotopic ratios of the trapped Ar components of Z102 pyroxene microinclusions and amphibole indeed reflect the argon isotopic composition of the fluid source rather than homogenization or equilibration of former different components.

The $^4He/^{40}Ar$ ratio of both inclusion types of Z31 orthopyroxene is close to ~0.16. As atmospheric contamination only marginally alters the ^4He and ^{40}Ar abundances, the radiogenic nuclides are mainly derived from the mantle, and their isotope ratio rather represents the indigenous noble gas abundance of the mantle fluid in the peridotite source. The ratio of these two radiogenic nuclides also can tell us something about the Earth's history. The global $^4He/^{40}Ar$ ratio of the mantle should be simply governed by the relative K, U, and Th abundances and the epoch and duration of accumulation of the radiogenic daughter products within the reservoir from which the rocks are derived. The current production rate is $^4He/^{40}Ar = 5.5$, accumulation over 4.5 Ga yields $^4He/^{40}Ar = 2.1$, for $Th/U = 3.3$, and $K/U = 10^4$ (Ozima and Podosek, 1983). Different values of $Th/U = 2.0$ and $K/U = 1.27 \times 10^4$ (Jochum et al., 1983) yield $^4He/^{40}Ar$ ratios of 3.6 and 2.3, respectively. If the upper mantle value is closer to the respective higher values, this would indicate recent production rates and would be suggestive of a massive early, not a continuous late degassing. However, the evaluation of the global upper mantle value is not so easy. Ocean ridge basalts exhibit sometimes $^4He/^{40}Ar$ ratios as high as 20 (Hamano and Ozima, 1978; Staudacher et al., 1989, Sarda et al., 1988). Values as high as 20 are not yet well understood. A promising explanation is solubility-controlled partitioning between a magma and a gas phase, the latter one being enriched in heavy noble gases, as solubility decreases with increasing mass of the noble gas atom. Jambon et al. (1985) found high $^4He/^{40}Ar$ values of ~6 in the vesicles of a MORB glass and an even higher ratio of ~12 in the glass phase. They explained this observation by differential noble gas partitioning associated with loss of primary vesicles. During ascent, the magma exsolves primary vesicles with a relatively low $^4He/^{40}Ar$ ratio (<1). These vesicles are lost leaving a fairly high bulk $^4He/^{40}Ar$ ratio between 6 and 12. The remaining magma continues exsolving vesicles during further ascent and retains the newly formed vesicles with $^4He/^{40}Ar$ ratios of about 6, while the remaining glass phase has then values of about 12. Similar mechanisms were advocated by Honda et al. (1993) to explain He enrichments with respect to Ne. The $^4He/^{40}Ar$ value for Zabargad rocks is rather constant around 0.15 for three samples and 0.30 for Z103G. Such low values also have been observed for ultramafic xenoliths (Gramlich and Naughton, 1972; Funkhouser and Naughton, 1968; Bernatowicz, 1981; Kyser and Rison, 1982). They neither reach maximum values like some of the upper mantle-derived ocean ridge basalts nor the expected mantle values between 2.1 and 5.5, thus pointing in the opposite direction when compared to MORB. Dunai and Baur (1995) also observed low $^4He/^{40}Ar$ values for a variety of xenoliths from the European subcontinental mantle. $^4He/^{40}Ar$ ratios correlated neither with $^{40}Ar/^{36}Ar$ nor $^3He/^4He$ ratios, so excluding addition of atmospheric Ar or simple diffusive He loss as reasons, respectively.

The observation that peridotitic rocks have systematically lower $^4He/^{40}Ar$ ratios than their host basalts (e.g., Funkhouser and Naughton, 1968; Kyser and Rison, 1982) or submarine basalts in general is difficult to interpret. Solubility-controlled partitioning may be a reasonable explanation, coupled with differential diffusivity of He and Ar under elevated mantle temperatures (e.g., Gramlich and Naughton, 1972). However, present state-of-knowledge does not allow to evaluate the exact fractionation mechanism. Experimental data suggest enrichment of the lighter noble gases in the melt phase during both crystal/melt- and vapor/melt-partitioning (Carroll et al., 1994; Shibata et al., 1994), but there are no partitioning experiments involving all three phases or solids and fluids that certainly interact simultaneously in the mantle. In any case the existence of fractionated fluids or melts in the peridotite source region seems to play an important role. As fractionation obviously takes place in the mantle, it becomes very unlikely to find a rock with an unfractionated $^4He/^{40}Ar$ ratio or to prove that a certain rock has such an unfractionated ratio.

5. SUMMARY AND CONCLUSIONS

Zabargad peridotites are upper mantle rocks which commonly are believed to have intruded the crust during the opening of the Red Sea 18–19 Ma ago. The main rocks of the three ultramafic bodies are spinel lherzolites with a chemical composition similar to that of unfractionated primitive upper mantle. In particular, the fact that the main rock type are spinel lherzolites with a REE pattern indistinguishable from primitive ultramafic xenoliths makes them unique among worldwide massive peridotite occurrences. Associated with the peridotites are (mostly monomineralic) vein rocks, such as clinopyroxenites, orthopyroxenites, websterites, hornblendites, plagioclasites, and olivinites. Their genesis has been related to the activity of fluid phases in the upper mantle during diapiric uplift of the Zabargad peridotites (Kurat et al., 1993).

An intrusion age of 18–19 Ma is consistent with the age of a late amphibole vein rock (Z28) that formed 18.7 ± 1.3 Ma ago at rather low temperatures by interaction with fluids derived from seawater. The same event affected plagioclasite vein Z13G, for which we obtain a minimum age of 16.7 ± 0.9 Ma. Z28 is the first Zabargad rock successfully dated with the ^{40}Ar-^{39}Ar technique. Clinopyroxenites Z102 and Z103G retained excess argon with $^{40}Ar/^{36}Ar$ ratios up to 8000 bearing the signature of mantle-derived rocks. High values of up to 30,000 are typical for upper mantle-derived MORB-glass (Sarda et al., 1985; Jambon et al., 1985; Staudacher et al., 1989), while for the undepleted mantle lower

values are assumed. Both noble gas components could be present along the Red Sea rift zone (Moreira et al., 1996) that in our case can only be tested by further isotopic He and Ne data. High resolution stepheating of neutron irradiated samples allowed detailed analysis of the degassing characteristics of the samples. Using the diffusion behaviour of K-, Ca-, and Cl-derived argon isotopes, different mineralogical phases were identified that contain trapped components of different isotopic composition. Important carriers are various generations of mantle amphiboles as described by Agrinier et al. (1993), which are related to different stages of diapiric uplift. They contain Ar with much higher $^{40}Ar/^{36}Ar$ ratios than the late stage amphibole Z28 ($^{40}Ar/^{36}Ar = 305$), which reflects trapping of Ar from the mantle source. In clinopyroxenite Z102, high temperature argon is trapped mainly within microinclusions, which also can be related to fluid activities in the mantle (Kurat et al., 1993). In clinopyroxenite Z103G, high temperature Ar is probably trapped mainly in the pyroxene lattice. Horizontal zero age arrays in Ar three-isotope-plots can be interpreted in a way, that formation of pyroxene microinclusions, amphiboles, and trapping of Ar are the result of recent mantle metasomatism. This metasomatism is also evident in ultramafic xenoliths from Arabian Cenozoic volcanic fields (Henjes-Kunst et al., 1990) and may have affected large parts of the lithospheric mantle beneath the Arabian-Nubian plate.

A suite of two vein rocks and their host rocks were also analyzed for ^{4}He, ^{20}Ne, ^{40}Ar, and ^{36}Ar. A stepwise crushing and subsequent total fusion experiment on orthopyroxenite vein rock Z31 yielded remarkable results. The correlation of isotopic ratios with increasing crushing step showed that stepcrushing is able to separate different noble gas components hosted by two different fluid inclusion types. They most probably can be identified as primary and secondary fluid inclusions. Both contain mantle ^{4}He and ^{40}Ar, while an isotope correlation plot of $^{36}Ar/^{40}Ar$ vs. $^{4}He/^{40}Ar$ clearly points to an atmospheric Ar component that was admixed to the mantle fluids in the peridotite source region. The $^{4}He/^{40}Ar$ ratio (0.12–0.30) of all rocks is too low to be explained alone by long term decay of radioactive parent nuclides U, Th, and K, but is genuine to the mantle source region of the Zabargad peridotitic rocks. Similarly low ratios had already been observed in upper mantle xenoliths, and they are most probably caused by fractionation processes in the mantle.

Recent mantle metasomatism was related to fluids that introduced Ar of distinctly different composition into amphiboles and fluid inclusions. These fluids are characterized to a certain extent via natural and neutron-induced argon isotopes that give some additional information on K and Cl. The fluids may have had a common progenitor but must have been modified repeatedly to account for differences in the phases and the inclusions formed by fluid rock-interaction. A possible scenario invokes a parent fluid with a relatively high $^{40}Ar/^{36}Ar$ ratio of ~6500 and $^{40}Ar_{exc}/Cl \sim 0.27$ that interacts with fluids carrying atmospheric argon and H_2O and K-bearing fluids, which is consistent with the formation conditions of type II amphibole as outlined by Agrinier et al. (1993). Within almost all phases derived from mantle fluids we found evidence for mixing of mantle and atmosphere-type noble gases. This implies deep circulating fluids and/or reworked (oceanic?) crust importing an atmospheric signature into the peridotite source region.

This investigation points to multiple trapped noble gas components due to multiple fluid-rock interactions. As the total fusion data yield an average value of noble gas isotopic and elemental ratios with doubtful significance, we stress the necessity to resolve the different components by appropriate experimental techniques like stepheating and stepcrushing of irradiated and nonirradiated samples. Observations of varying trapped argon isotope ratios are ubiquitous so far, however, definite associations with mineralogical phases are rarely established. Although some of the studies were carried out on mineral separates of ultramafic xenoliths, no high resolution measurements are available. There is also a lack of data on neutron-irradiated samples in order to resolve possible radiogenic components and, what is even more important, to tie Ar to specific major and minor (mineral) phases and to characterize Ar, K, and Cl signatures via the corresponding argon isotopes. Thus, this study should be regarded as an approach encouraging future high resolution ^{40}Ar-^{39}Ar and noble gas analysis of mantle-derived rocks in order to reveal multiple fluid-rock interactions leaving their specific noble gas isotopic fingerprint within these rocks.

Acknowledgments—We thank J. Oehm for sample preparation and handpicking of the mineral separates and A. ElGoresy for helpful discussions. Reviews of D. E. Fisher and J. Kunz improved the manuscript. MT acknowledges the support by the Deutsche Forschungsgemeinschaft and GK the support by the Austrian Fonds zur Förderung der wissenschaftlichen Forschung.

REFERENCES

Agrinier P., Mével C., Bosch D., and Javoy M. (1993) Metasomatic hydrous fluids in amphibole peridotites from Zabargad Island (Red Sea). *Earth Planet. Sci. Lett.* **120,** 187-205.

Allègre C. J., Staudacher Th., and Sarda P. (1986) Rare gas systematics: formation of the atmosphere, evolution, and structure of the Earth's mantle. *Earth Planet. Sci. Lett.* **81,** 127–150.

Berger G. W. (1975) $^{40}Ar/^{39}Ar$ step heating of thermally overprinted biotite, hornblende and potassium feldspar from Eldora, Colorado. *Earth Planet. Sci. Lett.* **26,** 387–408.

Bernatowicz T. J. (1981) Noble gases in ultramafic xenoliths from San Carlos, Arizona. *Contrib. Mineral. Petrol.* **76,** 84–91.

Bonatti E., Ottonello G., and Hamlyn P. R. (1986) Peridotites from the Island of Zabargad (St. John), Red Sea: Petrology and geochemistry. *J. Geophys. Res.* **91,** 599–631.

Boudier F. and Nicolas A. (1972) Fusion partielle gabbroique de la lherzolite de Lanzo. *Schweiz. Mineral. Petrogr. Mitt.* **52,** 39–56.

Boudreau A. E., Mathez E. A., and McCallum I. S. (1986) Halogen geochemistry of the Stillwater and Bushveld Complexes: Evidence for transport of the platinum group elements by Cl-rich fluids. *J. Petrol.* **27,** 967–986.

Bowen N. L. and Tuttle O. F. (1949) The system MgO-SiO_2-H_2O. *Geol. Soc. Amer. Bull.* **60,** 439–460.

Brandstätter F., Ntaflos T., and Kurat G. (1993) *Electron Microprobe Analyses of Minerals from Peridotites and Associated Vein Rocks of Zabargad Island, Red Sea, Egypt.* Spec. Publ. Min. Petr. Abt., Naturhist. Museum, Wien.

Brereton N. R. (1970) Corrections for interfering isotopes in the ^{40}Ar-^{39}Ar dating method. *Earth Planet. Sci. Lett.* **8,** 427–433.

Brueckner H. K., Zindler A., Seyler M., and Bonatti E. (1988) Zabargad and the isotopic evolution of the sub-Red Sea mantle and crust. *Tectonophysics* **150,** 163–176.

Brueckner H. K. et al. (1995) A Pan African origin and uplift for the gneisses and peridotites of Zabargad Island, Red Sea: A neodymium, strontium, lead, and osmium isotope study. *J. Geophys. Res.* **100,** 22,283–22,297.

Carroll M. R., Draper D. S., Brooker R. A., and Kelley S. (1994) Noble gas solubilities in Melts and Crystals. In *Noble Gas Geochemistry and Cosmochemistry* (ed. J. Matsuda), pp. 325–341. Terra Sci. Publ. Co.

Cawthorn R. G. (1975) The amphibole peridotite-metagabbro complex, Finero, northern Italy. *J. Geol.* **8,** 437–457.

Dunai T. J. and Baur H. (1995) Helium, neon, and argon systematics of the European subcontinental mantle: Implications for its geochemical evolution. *Geochim. Cosmochim. Acta* **59,** 2767–2783.

Dungan M. A. and AvéLallement H. G. (1977) Formation of small dunite bodies by metasomatic transformation of harzburgite in the Canyon Mountain ophiolite, northeast Oregon. In *Magma Genesis* (ed. H. J. B. Dick), pp. 109–128. Oregon Dept. Geol. Mineral Res. Bull

Farley K. A. and Craig H. (1994) Atmospheric argon contamination of ocean island basalt olivine phenocrysts. *Geochim. Cosmochim. Acta* **58,** 2509.

Fisher D. E. (1985) Noble gases from oceanic island basalts do not require an undepleted mantle source. *Nature* **316,** 716–718.

Fisher D. E. (1994) Mantle and atmosphere-like argon in vesicles of MORB glasses. *Earth Planet. Sci Lett.* **123,** 199–204.

Flohs I. (1979) ^{40}Ar-^{39}Ar-Datierung von Mineralseparaten gewöhnlicher Chondrite. Dipl. thesis, Univ. Heidelberg.

Frey F. A. (1980) The origin of pyroxenites and garnet-pyroxenites from Salt Lake Crater, Oahu, Hawaii: Trace element evidence. *Amer. J. Sci.* **280-A,** 427–449.

Fuhrmann U., Lippolt H. J., and Hess J. C.(1987) Examination of some proposed K-Ar standards: ^{40}Ar/^{39}Ar analyses and conventional K-Ar data. *Chem. Geol. (Isot. Geosci. Sect.)* **66,** 41–51.

Funkhouser J. G. and Naughton J. J. (1968) Radiogenic helium and argon in ultramafic inclusions from Hawaii. *J. Geophys. Res.* **73,** 4601–4607.

Gramlich J. W. and Naughton J. J. (1972) Nature of source material for ultramafic minerals from Salt Lake Crater, Hawaii, from measurements of helium and argon diffusion. *J. Geophys. Res.* **77,** 3032–3042.

Hamano Y. and Ozima M. (1978) Earth-atmosphere evolution model based on argon isotopic data. In *Terrestrial rare gases* (ed. E. C. Alexander Jr. and M. Ozima), pp. 155–171. Japan Sci. Soc. Press.

Hanson G. N., Simmons K. R., and Bence A. E. (1975) ^{40}Ar/^{39}Ar spectrum ages for biotite, hornblende, and muscovite in a contact metamorphic zone. *Geochim. Cosmocim. Acta* **39,** 1269–1277.

Harlow G. E. (1997) Potassium in clinopyroxene at high pressure and temperature: An experimental study. *Amer. Mineral.* **82,** 259–269.

Harrison T. M. and Fitz Gerald J. D. (1986). Exsolution in hornblende and its consequences for ^{40}Ar/^{39}Ar age spectra and closure temperature. *Geochim. Cosmochim. Acta* **50,** 247–253.

Harrison T. M. and McDougall I. (1981) Excess ^{40}Ar in metamorphic rocks from Broken Hill, New South Wales: Implications for ^{40}Ar-^{39}Ar age spectra and the thermal history of the region. *Earth Planet. Sci Lett.* **55,** 123–149.

Henjes-Kunst F., Altherr R., and Baumann A. (1990) Evolution and composition of the lithospheric mantle underneath the western Arabian peninsula: Constraints from Sr-Nd isotope systematics of mantle xenoliths. *Contrib. Mineral. Petrol.* **105,** 460–472

Hess H. H. (1969) *Stillwater igneous complex, Montana: A quantitative mineralogical study. Geol. Soc. Amer. Mem.* **80**

Hiyagon H., Ozima M., Marty B., Zashu S., and Sakai H. (1992) Noble gases in submarine glasses from mid-oceanic ridges and Loihi seamount: Constraints on the early history of the Earth. *Geochim. Cosmochim. Acta* **56,** 1301–1316.

Honda M., McDougall I., Patterson D. B., Doulgeris A., and Clague D. A. (1993). Noble gases in submarine pillow basalt glasses from Loihi and Kilauea, Hawaii: A solar component in the Earth. *Geochim. Cosmochim. Acta* **57,** 859–874.

Horn P., Jessberger E. K., Kirsten T., and Richter H. (1974) ^{39}Ar-^{40}Ar dating of lunar rocks: Effects of grain size and neutron irradiation. *Proc. 6th Lunar Planet. Sci. Conf.* , 1563–1591.

Huneke J. C. and Smith S. P. (1976) The realities of recoil: ^{39}Ar recoil out of small grains and anomalous age patterns in ^{40}Ar-^{39}Ar dating. *Proc. 7th Lunar Planet. Sci. Conf.* , 1987–2008.

Jagoutz E. et al. (1979). The abundances of major, minor, and trace elements in the Earth's mantle as derived from primitive ultramafic nodules. *Proc. 10th Lunar Planet. Sci. Conf.* , 2031–2050.

Jambon A., Weber H. W., and Begemann F. (1985) Helium and argon from an Atlantic MORB glass: Concentration, distribution, and isotopic composition. *Earth Planet. Sci Lett.* **73,** 255–267.

Jessberger E. K. (1977) Comments on: "Identification of excess-^{40}Ar by the ^{40}Ar-^{39}Ar spectrum technique" by M. A. Lanphere and G. B. Dalrymple. *Earth Planet. Sci. Lett.* **37,** 167.

Jessberger E. K. and Gentner W. (1972) Mass spectrometric analysis of gas inclusions in Muong Nong glass and Libyan Desert glass. *Earth Planet. Sci. Lett.* **14,** 221–225.

Jessberger E. K., Huneke J. C., Podosek F. A., and Wasserburg G. J. (1974) High resolution argon analysis of neutron irradiated Apollo 16 rocks and separated minerals. *Proc. 5th Lunar Planet. Sci. Conf.* , 1419.

Jessberger E. K., Dominik B., Staudacher Th., and Herzog G. F. (1980) ^{40}Ar-^{39}Ar ages of Allende. *Icarus* **42,** 380–405.

Jochum K. P., Hofmann A. W., Ito E., Seufert H. M., and White W. M. (1983) Krypton, uranium, and thorium in mid-ocean ridge basalt glasses and heat production, K/U, and K/Rb in the mantle. *Nature* **306,** 431.

Kaneoka I. and Takaoka N. (1978) Excess ^{129}Xe and high ^{3}He/^{4}He ratios in olivine phenocrysts of Kapuho Lava and xenolithic dunites from Hawaii. *Earth Planet. Sci. Lett.* **39,** 382–386.

Kaneoka I., Takaoka N., and Aoki K. (1978) Rare gases in mantle-derived rocks and minerals. In *Terrestrial Rare Gases* (ed. E. C. Alexander Jr. and M. Ozima), pp. 71–83. Japan Sci. Soc. Press.

Kaneoka I., Takaoka N., and Clague D. A. (1983) Noble gas systematics for coexisting glass and olivine crystals in basalts and dunite xenoliths from Loihi Seamount. *Earth Planet. Sci. Lett.* **66,** 427–437.

Kawahata H., Kusabe M., and Kikuchi Y. (1987) Strontium, oxygen, and hydrogen isotope geochemistry of hydrothermally altered and weathered rocks in DSDP hole 504B Costa-Rica rift. *Earth Planet. Sci. Lett.* **85,** 343–555.

Kurat G. et al. (1993) Petrology and geochemistry of peridotites and associated vein rocks of Zabargad island, Red Sea, Egypt. *Mineral. Petrol.* **48,** 309–341.

Kyser T. K. and Rison W. (1982) Systematics of rare gas isotopes in basic lavas and ultramafic xenoliths. *J. Geophys. Res.* **87,** 5611–5630.

Lanphere M. A. and Dalrymple G. B. (1976) Identification of excess Argon by the ^{40}Ar-^{39}Ar age spectrum technique. *Earth Planet. Sci. Lett.* **32,** 141–148.

Loomis T. P. and Gottschalk R. R. (1981) Hydrothermal origin of mafic layers in alpine-type peridotites: Evidence from the Seiad Ultramafic Complex, California, USA. *Contrib. Mineral. Petrol.* **76,** 1–11

Lopez-Martinez M., York D., and Hanes J. A. (1992) A ^{40}Ar-^{39}Ar geochronological study of komatiites and komatiitic basalts from the Lower Onverwacht Volcanics, Barberton Mountain Land, South Africa. *Precambrian Res.* **57,** 91.

Marty B. and Ozima M. (1986) Noble gas distribution in oceanic basalt glasses. *Geochim. Cosmochim. Acta* **50** 1093–1097.

Matsuda J. and Marty B. (1995) The ^{40}Ar /^{36}Ar ratio of the undepleted mantle; A reevaluation. *Geophys. Res. Lett.* **22,** 1937–1940.

Moreira M., Valbracht P. J., Staudacher Th., and Allegre C. J. (1996) Rare gas systematics in Red Sea ridge basalts. *Geophys. Res. Lett.* **23,** 2453–2456.

Nicolas A., Boudier F., Lyberis N., Montigny R., and Guennoc P. (1985) Zabargad (St. John) Island: A key witness of early rifting in the Red Sea. *CR Acad. Sci. Paris* **II,** 1063–1068.

Nicolas A., Boudier F., and Montigny R. (1987) Structure of Zabargad Island and early rifting of the Red Sea. *J. Geophys. Res.* **92,** 461–474.

Oberli R., Ntaflos T., Meier M., and Kurat G. (1987) Emplacement age of the peridotites from Zabargad Island (Red Sea): A zircon U-Pb isotope study. Terra Cognita **7,** 334.

Onstott T. C. and Peacock M. W. (1987) Argon retentivities of hornblendes: A field experiment in a slowly cooled metamorphic terrane. *Geochim. Cosmochim. Acta* **51,** 2891–2903.

Ozima M. (1975). Argon isotopes and Earth-atmosphere evolution models. *Geochim. Cosmochim. Acta* **39,** 1127–1134.

Ozima M. and Podosek F. A. (1983) *Noble gas geochemistry*. Cambridge Univ. Press.

Patterson D. B., Honda M., and McDougall I. (1990) Atmospheric contamination: A possible source for heavy noble gases in basalts from Loihi seamount, Hawaii. *Geophys. Res. Lett.* **17,** 705–708.

Piccardo G. B., Rampone E., Vannucci R., Shimizu N., Ottolini L., and Bottazzi P. (1993) Mantle Processes in the Sub-Continental Lithosphere—the Case Study of the Rifted Sp-Lherzolites from Zabargad (Red Sea). *European J. Mineral.* **5,** 1039–1056.

Poreda R.J. and Farley K.A. (1992) Rare gases in Samoan xenoliths. *Earth Planet. Sci. Lett.* **113,** 129–144.

Sarda P., Staudacher Th., and Allègre C. J. (1985) $^{40}Ar/^{36}Ar$ in MORB glasses: Constraints on atmosphere and mantle evolution. *Earth and Planet. Sci. Lett.* **72,** 357.

Schaeffer G. A. and Schaeffer O. A. (1977) ^{40}Ar-^{39}Ar ages of lunar rocks. *Proc. 8th Lunar Planet. Sci. Conf.* , 2253–2300.

Schiffries C. M. and Skinner B. J. (1987) The Bushveld hydrothermal system: Field and petrologic evidence. *Amer. J. Sci.* **287,** 566–595.

Shibata T., Takahashi E., and Ozima M. (1994) Noble gas partition between basaltic melt and olivine crystals at high pressures. In *Noble Gas Geochemistry and Cosmochemistry* (ed. J. Matsuda), pp. 343–354. Terra Sci. Publ. Co..

Staudacher Th., Jessberger E. K., Dörflinger D., and Kiko J. (1978) A refined ultrahigh-vacuum furnace for rare gas analysis. *J. Phys. E. Sci. Instrum.* **11,** 781–784.

Staudacher Th., Kurz M. D., and Allègre C. J. (1986) New noble gas data in glass samples from Loihi seamount and Hualaaii and in dunite samples from Loihi and Reunion islands. *Chem. Geol.* **56,** 193.

Staudacher Th., Sarda P., Richardson S. H., Allègre C. J., Sagna I., and Dmitriev L. V. (1989) Noble gases in basalt glasses from a Mid-Atlantic Ridge topographic high at 14°N: Geodynamic consequences. *Earth Planet. Sci. Lett.* **96,** 119–133.

Steiger R. H. and Jäger E. (1977) Subcommission on Geochronology: Convention on the use of decay constants in geo- and cosmochronology. *Earth Planet. Sci. Lett.* **36,** 359–362.

Stettler A., Eberhardt P., Geiss J., Grögler N., and Maurer P. (1974) On the duration of lava flow activity in Mare Tranquillitatis. *Proc. 5th Lunar Planet. Sci. Conf.* , 1557–1570.

Trieloff M. (1990) ^{40}Ar-^{39}Ar Alter von LL-Chondriten. Dipl. Thesis, Univ. Heidelberg.

Trieloff M. (1993) Datierung impaktmetamorpher Gesteine und methodische Ergänzungen zur ^{40}Ar-^{39}Ar Altersbestimmungstechnik. PhD. Thesis, Univ. Heidelberg.

Trieloff M., Reimold W. U., Kunz J., Boer R. H., and Jessberger E. K. (1994) ^{40}Ar-^{39}Ar thermochronology of pseudotachylites at the Ventersdorp Contact Reef, Witwatersrand Basin. *S. Afr. J. Geol.* **97,** 365–384.

Turner G. (1971) Argon 40-Argon 39 Dating: The Optimization of Irradiation Parameters. *Earth Planet. Sci. Lett.* **10,** 227–234.

Turner G. and Cadogan P. H. (1974) Possible effects of ^{39}Ar recoil in ^{40}Ar-^{39}Ar dating. *Proc. 5th Lunar Planet. Sci. Conf.* , 1601–1615.

Turner G., Huneke J. C., Podosek F. A., and Wasserburg G. J. (1972) Ar^{40}-Ar^{39} systematics in rocks and separated minerals from Apollo 14. *Proc. 3th Lunar Planet. Sci. Conf.*, 1589–1612.

Turner G., Burgess R., and Bannon M. (1990) Volatile-rich mantle fluids inferred from inclusions in diamond and mantle xenoliths. *Nature* **344,** 653–655.

Villa I. M. (1990) ^{40}Ar-/^{39}Ar dating of amphiboles from Zabargad Island (Red Sea) is precluded by interaction with fluids. *Tectonophysics* **180,** 369–373.

Weber H. W., Braun O., Schultz L., and Begemann F. (1983) The noble gas record in antarctic and other meteorites. *Z. Naturforsch.* **38a,** 267.

Wilshire H. G., McGuire A. V., Noller J. S., and Turrin B. D. (1991) Petrology of lower crustal and upper mantle xenoliths from the Cima volcanic field, California. *J. Petrol.* **32,** 169–200.

APPENDIX

Tables A1–A6 contain the measured argon isotopes corrected for mass discrimination, sensitivity, system blanks, decay, and relative neutron doses. All isotopes are also corrected for interfering isotopes produced on K and Ca during irradiation. Remaining Ar isotopes have the following composition:

$^{36}Ar = {}^{36}Ar_{exc} + {}^{36}Ar_{atm}$

$^{37}Ar = {}^{37}Ar_{Ca}$

$^{38}Ar = {}^{38}Ar_{exc} + {}^{38}Ar_{atm} + {}^{38}Ar_{Cl}$

$^{39}Ar = {}^{39}Ar_{K}$

$^{40}Ar = {}^{40}Ar_{rad} + {}^{40}Ar_{exc} + {}^{40}Ar_{atm}$

exc: excess (or non-atmospheric, trapped) argon
atm: atmospheric argon
Ca: argon derived from Ca
Cl: argon derived from Cl
K: argon derived from K
rad: in situ radiogenic argon

Table A1. Zabargad Hornblende Z28 #1 J = (2.916 ± 0.027) × 10^{-4}.

Temp [°C]	^{36}Ar $\times10^{-12}$	^{37}Ar $\times10^{-11}$	^{38}Ar $\times10^{-13}$	^{39}Ar $\times10^{-12}$	^{40}Ar $\times10^{-10}$	Age [Ma]
400	48 ± 1	12 ± 4	84 ± 3	2 ± 1	137 ± 1	0.0 ± 0.0
600	607 ± 9	56 ± 6	1255 ± 15	10 ± 2	1816 ± 4	107 ± 121
750	643 ± 9	73 ± 7	1493 ± 21	12 ± 2	1985 ± 3	343 ± 120
960	915 ± 13	447 ± 9	3028 ± 27	181 ± 4	2838 ± 4	39 ± 11
1020	720 ± 10	1822 ± 24	6704 ± 54	669 ± 5	2444 ± 6	24.8 ± 2.4
1040	329 ± 5	1674 ± 23	5017 ± 42	579 ± 5	1220 ± 4	22.5 ± 1.4
1060	268 ± 2	1668 ± 13	4866 ± 23	565 ± 5	1019 ± 4	21.0 ± 0.7
1080	171 ± 2	1852 ± 16	4811 ± 25	606 ± 5	724 ± 4	18.9 ± 0.7
1100	26 ± 2	982 ± 16	2187 ± 17	307 ± 5	163 ± 4	14.6 ± 1.1
1120	11 ± 2	329 ± 6	646 ± 7	97 ± 5	53 ± 4	10.9 ± 3.4
1140	12 ± 2	106 ± 5	287 ± 5	40 ± 5	43 ± 4	8.2 ± 8.8
1200	14 ± 2	103 ± 4	264 ± 6	40 ± 5	45 ± 5	6.1 ± 9.6
1350	21 ± 3	252 ± 7	616 ± 8	91 ± 8	83 ± 8	11.3 ± 6.5
1600	12 ± 12	16 ± 16	74 ± 22	59 ± 37	35 ± 35	1.0 ± 44.0
1600	3 ± 3	—	9 ± 9	—	5 ± 5	0.0 ± 0.0
TOTAL	3800 ± 25	9392 ± 48	31340 ± 91	3259 ± 41	12609 ± 39	22.29 ± 1.40

Table A2. Zabargad Plagioclase Z13G #1 J = (2.916 ± 0.027) × 10^{-4}.

Temp [°C]	^{36}Ar $\times10^{-13}$	^{37}Ar $\times10^{-12}$	^{38}Ar $\times10^{-13}$	^{39}Ar $\times10^{-13}$	^{40}Ar $\times10^{-10}$	Age [Ma]
400	48 ± 5	2 ± 2	11 ± 2	7 ± 7	224 ± 1	4126 ± 2242
580	3142 ± 65	2523 ± 78	633 ± 10	2097 ± 21	4340 ± 6	700.3 ± 6.5
690	973 ± 23	5530 ± 110	125 ± 4	1516 ± 21	1430 ± 2	358.5 ± 4.9
750	1131 ± 12	4391 ± 47	174 ± 5	790 ± 17	724 ± 2	242.5 ± 5.4
800	1095 ± 11	7526 ± 89	110 ± 4	1273 ± 19	649 ± 2	129.6 ± 2.3
840	421 ± 8	9612 ± 98	—	1603 ± 20	304 ± 2	58.0 ± 1.1
870	297 ± 7	9639 ± 97	—	1580 ± 21	163 ± 2	24.8 ± 0.9
900	180 ± 7	8850 ± 100	—	1469 ± 20	100 ± 2	16.7 ± 0.9
930	93 ± 7	6310 ± 110	—	1122 ± 21	67 ± 2	18.5 ± 1.3
960	60 ± 7	4503 ± 51	—	881 ± 20	55 ± 2	22.2 ± 1.6
1000	69 ± 7	3864 ± 57	—	836 ± 21	93 ± 2	45.0 ± 2.0
1060	111 ± 8	3622 ± 55	—	912 ± 23	255 ± 2	124.0 ± 3.5
1150	154 ± 10	3928 ± 49	—	906 ± 30	1090 ± 3	523 ± 15
1300	280 ± 15	7150 ± 120	—	1025 ± 46	1741 ± 5	697 ± 26
1600	418 ± 73	15550 ± 270	—	3020 ± 220	1766 ± 21	265 ± 19
1600	32 ± 32	—	7 ± 7	—	13 ± 13	0.0 ± 0.0
TOTAL	8500 ± 110	93000 ± 410	1060 ± 14	19040 ± 240	13015 ± 27	269.0 ± 10.5

Table A3. Zabargad Hornblende Z28 #2 J = 0.01200 ± 0.00003.

Temp [°C]	^{36}Ar $\times10^{-12}$	^{37}Ar $\times10^{-10}$	^{38}Ar $\times10^{-11}$	^{39}Ar $\times10^{-11}$	^{40}Ar $\times10^{-10}$	Age [Ma]
300	18 ± 2	—	—	—	56 ± 6	1323 ± 3632
360	96 ± 3	—	3 ± 1	1 ± 1	285 ± 6	506 ± 1634
420	136 ± 4	9 ± 4	6 ± 1	2 ± 1	430 ± 6	1569 ± 531
480	169 ± 4	11 ± 3	8 ± 1	6 ± 1	524 ± 6	698 ± 352
540	138 ± 4	17 ± 3	9 ± 1	7 ± 1	416 ± 6	223 ± 414
600	230 ± 4	38 ± 4	24 ± 1	11 ± 1	728 ± 6	765 ± 190
660	252 ± 6	36 ± 4	45 ± 1	24 ± 1	814 ± 6	550 ± 119
720	143 ± 4	17 ± 4	45 ± 1	15 ± 1	465 ± 6	526 ± 144
780	148 ± 4	9 ± 3	50 ± 1	15 ± 1	499 ± 6	739 ± 123
840	126 ± 4	26 ± 3	45 ± 1	22 ± 1	425 ± 6	467 ± 99
900	107 ± 3	17 ± 5	35 ± 1	40 ± 1	349 ± 6	176 ± 54

Table A3 (Continued)

Temp [°C]	^{36}Ar $\times10^{-12}$	^{37}Ar $\times10^{-10}$	^{38}Ar $\times10^{-11}$	^{39}Ar $\times10^{-11}$	^{40}Ar $\times10^{-10}$	Age [Ma]
960	139 ± 4	65 ± 4	41 ± 1	80 ± 1	429 ± 6	49 ± 3
1020	251 ± 6	954 ± 15	399 ± 4	439 ± 2	797 ± 7	27 ± 9
1080	1731 ± 16	10616 ± 45	4913 ± 10	4412 ± 8	5855 ± 33	36.6 ± 2.8
1140	273 ± 14	12695 ± 49	4603 ± 10	4764 ± 10	1157 ± 39	16.5 ± 2.6
1200	14 ± 3	402 ± 10	144 ± 2	162 ± 2	43 ± 10	1.9 ± 18.5
1260	—	111 ± 9	42 ± 1	48 ± 1	—	0.0 ± 0.0
1320	15 ± 4	335 ± 10	115 ± 1	130 ± 1	63 ± 12	30 ± 28
1390	22 ± 5	169 ± 7	60 ± 1	65 ± 1	64 ± 15	0.0 ± 0.0
1460	28 ± 7	45 ± 6	14 ± 1	15 ± 1	92 ± 20	120 ± 388
1550	33 ± 20	2 ± 2	6 ± 1	2 ± 1	135 ± 62	2100 ± 2838
TOTAL	4070 ± 34	25576 ± 72	10609 ± 15	10258 ± 13	13625 ± 89	34.0 ± 2.8

Table A4. Zabargad Plagioclase Z13G #2 J = 0.01200 ± 0.00003.

Temp [°C]	^{36}Ar $\times10^{-12}$	^{37}Ar $\times10^{-10}$	^{38}Ar $\times10^{-12}$	^{39}Ar $\times10^{-12}$	^{40}Ar $\times10^{-9}$	Age [Ma]
300	18 ± 4	—	12 ± 2	48 ± 2	5 ± 1	57 ± 735
360	120 ± 5	17 ± 5	106 ± 2	669 ± 7	39 ± 1	112 ± 57
420	198 ± 6	45 ± 5	213 ± 4	1482 ± 8	66 ± 1	114 ± 29
480	235 ± 6	67 ± 4	226 ± 4	2242 ± 14	91 ± 1	194 ± 19
540	240 ± 7	95 ± 6	203 ± 5	3073 ± 19	114 ± 1	279 ± 14
600	212 ± 6	156 ± 6	173 ± 4	3366 ± 18	136 ± 1	417 ± 11
660	106 ± 5	266 ± 7	97 ± 3	2541 ± 17	81 ± 1	384 ± 13
720	84 ± 5	577 ± 13	84 ± 3	2195 ± 13	53 ± 1	257 ± 16
780	178 ± 7	1255 ± 23	148 ± 4	2836 ± 16	68 ± 1	113 ± 18
840	114 ± 6	2171 ± 33	89 ± 3	4383 ± 26	53 ± 1	93 ± 11
900	111 ± 8	3999 ± 59	81 ± 4	7512 ± 41	48 ± 2	43.3 ± 8
960	67 ± 7	4546 ± 29	36 ± 4	8553 ± 28	24 ± 2	10 ± 8
1020	33 ± 6	2884 ± 45	24 ± 3	5837 ± 35	17 ± 1	26 ± 8
1080	36 ± 6	2540 ± 40	27 ± 3	5431 ± 31	41 ± 1	117 ± 9
1140	50 ± 6	2257 ± 31	15 ± 3	3932 ± 20	106 ± 1	441 ± 9
1200	46 ± 6	2128 ± 34	13 ± 3	3351 ± 19	111 ± 1	540 ± 11
1260	18 ± 4	659 ± 10	15 ± 2	975 ± 6	26 ± 1	409 ± 31
1320	27 ± 5	916 ± 13	20 ± 3	1341 ± 10	32 ± 1	351 ± 24
1390	21 ± 6	531 ± 12	16 ± 3	750 ± 7	21 ± 2	391 ± 56
1460	23 ± 7	698 ± 13	8 ± 3	974 ± 8	33 ± 2	501 ± 53
1550	102 ± 10	2294 ± 30	60 ± 5	3525 ± 24	97 ± 3	372 ± 21
TOTAL	2039 ± 28	28100 ± 120	1665 ± 16	65016 ± 93	1262 ± 7	207.2 ± 3.3

Table A5. Zabargad Clinopyroxene Z102 J = 01200 ± 0.00003.

Temp [°C]	^{36}Ar $\times10^{-13}$	^{37}Ar $\times10^{-10}$	^{38}Ar $\times10^{-12}$	^{39}Ar $\times10^{-12}$	^{40}Ar $\times10^{-10}$	Age [Ma]
290	157 ± 10	1 ± 1	53 ± 1	23 ± 1	71 ± 2	1.492 ± 0.152
360	231 ± 11	4 ± 2	92 ± 2	47 ± 1	129 ± 2	1.691 ± 0.073
420	217 ± 9	—	112 ± 2	66 ± 1	158 ± 2	1.788 ± 0.045
480	176 ± 11	5 ± 2	141 ± 2	79 ± 1	217 ± 2	2.255 ± 0.035
540	50 ± 4	2 ± 1	48 ± 1	16 ± 1	58 ± 1	2.598 ± 0.066
620	6810 ± 120	50 ± 33	1266 ± 12	215 ± 4	3155 ± 2	3.606 ± 0.056
680	5276 ± 98	115 ± 36	1506 ± 14	317 ± 5	2972 ± 2	3.335 ± 0.038
740	2134 ± 43	60 ± 15	1237 ± 12	247 ± 3	2146 ± 2	3.831 ± 0.023
800	2040 ± 44	39 ± 28	1052 ± 11	380 ± 4	1945 ± 2	2.985 ± 0.022
860	1319 ± 27	83 ± 38	1238 ± 11	485 ± 5	2080 ± 2	2.966 ± 0.017
920	808 ± 21	—	669 ± 6	333 ± 3	1967 ± 2	3.567 ± 0.016
980	803 ± 23	65 ± 37	452 ± 4	275 ± 4	1589 ± 2	3.485 ± 0.024
1040	1468 ± 33	246 ± 47	1491 ± 14	1310 ± 8	2290 ± 2	1.792 ± 0.009
1100	2468 ± 55	857 ± 55	3215 ± 31	2935 ± 16	2776 ± 3	1.097 ± 0.008
1170	837 ± 26	938 ± 55	1000 ± 10	808 ± 8	1277 ± 3	1.673 ± 0.014
1240	1968 ± 51	1518 ± 52	2393 ± 22	1619 ± 10	2350 ± 5	1.511 ± 0.011
1310	4850 ± 280	19000 ± 270	6861 ± 62	3748 ± 35	7421 ± 57	1.931 ± 0.023
1380	1340 ± 170	12650 ± 180	2177 ± 21	1029 ± 20	1417 ± 38	1.414 ± 0.062
1460	171 ± 15	817 ± 50	190 ± 2	105 ± 5	204 ± 4	1.832 ± 0.072
1560	77 ± 17	35 ± 29	7 ± 1	8 ± 3	52 ± 3	2.991 ± 0.620
1540	51 ± 14	—	3 ± 1	5 ± 1	21 ± 3	1.624 ± 0.950
TOTAL	33250 ± 380	36490 ± 360	25203 ± 82	14051 ± 48	34294 ± 70	2.035 ± 0.008

Table A6. Zabargad Clinopyroxene Z103G J = 0.1200 ± 0.00003.

Temp [°C]	^{36}Ar $\times10^{-13}$	^{37}Ar $\times10^{-10}$	^{38}Ar $\times10^{-13}$	^{39}Ar $\times10^{-13}$	^{40}Ar $\times10^{-10}$	Age [Ma]
300	19 ± 7	—	86 ± 6	11 ± 11	8 ± 2	2.507 ± 2.024
380	127 ± 9	11 ± 1	2288 ± 32	175 ± 8	96 ± 2	2.903 ± 0.106
460	146 ± 9	33 ± 2	3844 ± 52	390 ± 9	175 ± 2	2.927 ± 0.050
530	162 ± 10	49 ± 3	3097 ± 44	430 ± 11	225 ± 2	3.216 ± 0.048
600	211 ± 11	117 ± 3	2919 ± 39	528 ± 11	466 ± 2	4.184 ± 0.038
670	348 ± 16	178 ± 5	3079 ± 42	686 ± 16	660 ± 2	4.282 ± 0.041
730	109 ± 9	189 ± 5	1424 ± 23	398 ± 11	306 ± 2	4.014 ± 0.047
790	114 ± 12	344 ± 8	1824 ± 29	564 ± 14	310 ± 2	3.481 ± 0.046
850	89 ± 13	494 ± 10	1729 ± 24	800 ± 19	409 ± 2	3.443 ± 0.040
900	78 ± 11	468 ± 5	1823 ± 14	729 ± 13	524 ± 2	4.013 ± 0.031
940	59 ± 11	395 ± 4	773 ± 11	625 ± 12	349 ± 2	3.601 ± 0.035
990	61 ± 10	467 ± 5	1695 ± 15	1441 ± 17	412 ± 2	2.621 ± 0.021
1040	82 ± 11	510 ± 6	6346 ± 32	5334 ± 20	482 ± 3	1.276 ± 0.009
1090	79 ± 14	509 ± 8	5296 ± 29	3759 ± 25	590 ± 3	1.862 ± 0.013
1140	78 ± 15	828 ± 8	3057 ± 23	1924 ± 16	484 ± 4	2.442 ± 0.020
1200	188 ± 32	2678 ± 24	5725 ± 40	2572 ± 34	859 ± 9	2.810 ± 0.030
1260	135 ± 37	3046 ± 24	5001 ± 39	1413 ± 31	744 ± 10	3.504 ± 0.047
1320	400 ± 140	13206 ± 94	10228 ± 67	2000 ± 100	2328 ± 40	4.794 ± 0.097
1390	430 ± 120	11335 ± 82	7694 ± 53	1377 ± 99	984 ± 34	3.854 ± 0.147
1460	491 ± 27	960 ± 9	1409 ± 19	324 ± 17	324 ± 7	3.663 ± 0.126
1550	410 ± 65	125 ± 7	790 ± 33	199 ± 11	164 ± 21	2.313 ± 0.853
1600	151 ± 74	21 ± 8	250 ± 36	5 ± 5	56 ± 24	5.889 ± 6.171
TOTAL	3970 ± 230	35960 ± 130	70380 ± 170	25680 ± 160	10955 ± 64	3.098 ± 0.028